PONTIFICIA UNIVERSIDAD CATOLICA DE CHILE
SCHOOL OF ENGINEERING

NUMERICAL MODELING OF HYDROKINETIC TURBINES USING ACTUATOR DISKS: FLOW INTERACTION AND UPSCALING TO REGIONAL MODELS

DOMENICO ANDRÉS SCIOLLA PIÑEYRO

Thesis submitted to the Office of Research and Graduate Studies
in partial fulfillment of the requirements for the degree of
Master of Science in Engineering

Advisor:
CRISTIAN ESCAURIAZA

Santiago de Chile, September 2012

PONTIFICIA UNIVERSIDAD CATOLICA DE CHILE
SCHOOL OF ENGINEERING

NUMERICAL MODELING OF HYDROKINETIC TURBINES USING ACTUATOR DISKS: FLOW INTERACTION AND UPSCALING TO REGIONAL MODELS

DOMENICO ANDRÉS SCIOLLA PIÑEYRO

Members of the Committee:
CRISTIAN ESCAURIAZA
RODRIGO CIENFUEGOS
JOSÉ MIGUEL ARRIAZA
RICARDO PEREZ

Thesis submitted to the Office of Research and Graduate Studies
in partial fulfillment of the requirements for the degree of
Master of Science in Engineering

Santiago de Chile, September 2012

Gratefully to my parents and my wife Alessandra

ACKNOWLEDGEMENTS

Acknowledgements to HydroChile S.A. for the postgraduate scholarship in renewable energy, the FONDEF D09I1052 project, to Juan M. Veliz for his help with the computational resources, to Rodrigo Cienfuegos for introducing me into marine energy investigations and Cristian Escauriaza, my Advisor for leading the process.

TABLE OF CONTENTS

LIST OF FIGURES

LIST OF TABLES

ABSTRACT

The development of new technologies to harness energy from tidal currents in coastal areas requires an in-depth understanding of the interactions between the three-dimensional (3D) natural flow over arbitrary bathymetries and the marine hydrokinetic (MHK) turbines that can be potentially installed at a specific site. The optimal design of turbine farms and the evaluation of their environmental impacts require a multi-scale approach to analyze the effects, from a local scale in the vicinity of the devices to a larger scale comprising the entire coastal region affected by them. In spite of recent advances in the study of the flow hydrodynamics in the presence of turbine arrays, there is still the need to develop numerical models capable of resolving the wakes generated by multiple devices in high Reynolds number turbulent flows, capturing their interactions with the complex geometries of real aquatic environments and using affordable computational resources. In this investigation we simulate the 3D flow past porous disks using a hybrid turbulence model that combines Reynolds-averaged with large-eddy simulation (URANS/LES). We carry out numerical computations using the detached-eddy simulation approach (DES) (Spalart, Jou, Strelets, & Allmaras, 1997; Spalart, 2009) for the experimental configuration of Myers and Bahaj (2010, 2012). The results show that the model reproduces accurately the mean flow and turbulence statistics of the wakes generated by the momentum introduced by the disks, including the spatial distribution and characteristic scales of the turbulent coherent structures of sizes comparable to the devices. This model constitutes a powerful tool for analyzing in detail the flow field in realistic conditions and for estimating the power that can be extracted under different configurations using low computational resources. In addition, the simulation results are employed to determine the forces induced by the turbine array on the entire flow, parameterizing its effects to be incorporated in regional-scale models by using time and spatial averaging techniques.

Keywords: marine energy, hydrokinetic turbines, actuator disks, numerical 3D models.

RESUMEN

El desarrollo de nuevas tecnologías para aprovechar la energía de las corrientes de marea en las zonas costeras, requiere una comprensión en profundidad de las interacciones entre el flujo natural en las tres dimensiones (3D) sobre batimetrías arbitrarias y las turbinas marinas hidrocinéticas (MHK), que se podrían instalar en un sitio específico. El diseño óptimo de las granjas de turbinas y la evaluación de sus impactos ambientales requiere un enfoque en múltiples escalas para analizar los efectos, a partir de una escala local en las proximidades de los dispositivos hasta una escala mayor que comprende toda la región costera afectada. A pesar de los recientes avances en el estudio de la hidrodinámica del flujo en la presencia de conjuntos de turbinas, todavía existe la necesidad de desarrollar modelos numéricos capaces de resolver las estelas generadas por múltiples dispositivos en flujos turbulentos con altos números de Reynolds, capturando las interacciones con geometrías complejas presentes en los ambientes acuáticos reales, utilizando recursos computacionales asequibles. En esta investigación se simula el flujo 3D pasando por discos porosos, usando un modelo híbrido de turbulencia que combina el promedio de Reynolds, con la simulación de remolinos grandes (URANS / LES). Llevamos a cabo los cálculos numéricos utilizando el método de simulación de remolinos separados (DES) (Spalart et al., 1997; Spalart, 2009) para la configuración experimental de Myers y Bahaj (2010,2012). Los resultados muestran que el modelo reproduce con precisión el caudal medio y las estadísticas de la turbulencia de las estelas generadas por la cantidad de movimiento introducido por los discos, incluyendo la distribución espacial y las escalas características de las estructuras coherentes turbulentas, de tamaños comparables a los del dispositivos. Este modelo constituye una herramienta poderosa para analizar en detalle el campo de flujo en condiciones realistas y para la estimación de la potencia que puede ser extraída, en diferentes configuraciones, utilizando bajos recursos computacionales. Además, los resultados de la simulación se emplean para determinar las fuerzas inducidas por la granja de turbinas en todo el flujo,

parametrizando sus efectos para ser incorporados en modelos de escala regional, usando técnicas de promedio temporales y espaciales.

Palabras Claves: energía marina, turbinas hidrocinéticas, discos actuadores, modelos numéricos 3D.

1. INTRODUCTION

Technologies for extracting energy from tidal currents using hydrokinetic devices have not yet reached a full state of maturity to be incorporated extensively on power grid interconnected systems (Khan et al., 2008; Güney & Kaygusuz, 2010). Recent studies have identified the potential of many coastal areas that can provide significant energy resources in the near future, but their implementation will require to overcome challenging technical, environmental and economical aspects which are also specific for each site. Along the 6,400 km coast of Chile in the south Pacific Ocean, for example, the particular coastal morphology of the Chacao channel that separates the Chiloe island from the main continent (around $41°47'$ S, $73°31'$ W) has been identified as an important energy source that can potentially contribute a total power capacity between 600 and 800 MW, according to initial estimations (Garrad-Hassan, n.d.). In addition, new laws and regulations will also require a larger percentage of the energy portfolio produced from renewable sources to provide clean and more reliable energy to the system (Barroso, Rudnick, Sensfuss, & Linares, 2010). Motivated by the need to learn more about the physical and environmental processes that occur in this area, we are carrying out a comprehensive study in the Chacao channel that will include detailed field measurements, laboratory experiments of devices in physical models, and numerical simulations of flow past turbines for a wide range of scales to optimize the turbine arrays and evaluate their environmental effects.

The greatest difficulty for the numerical simulations, however, arises from the complex interactions that occur among the marine hydrokinetic (MHK) turbines, and their local and large-scale impacts they produce in the environment of the entire coastal region. The optimal installation of MHK devices depends considerably on the turbulent wakes that are generated and control the interaction within the turbine arrays and the natural arbitrary bathymetry. Environmental impacts are closely linked to the flow field generated by multiple devices, which can alter the local and regional hydrodynamic conditions, the sediment transport rates and erosion, and can also affect the ecosystem due to the total energy extraction and other chemical, acoustic, and electromagnetic effects ("polagye10", 2010). Recent numerical simulations of flow past MHK turbines have adopted different approaches for dealing with the complexity of these turbulent flows. Turbine design and local analysis of the flow fields require a detailed representation of the turbine blades with very high resolutions to resolve the flow hydrodynamics around the geometrical features of the turbine. This approach has been adopted for detailed simulations of single wind turbines, performing unsteady Reynolds-averaged Navier-Stokes (URANS) (Zahle & Sørensen, 2011) and large-eddy simulations (LES) (Sezer-Uzol & Long, 2006) of rotating devices. For MHK devices, Kang et al. (Kang, Borazjani, Colby, & Sotiropoulos, 2012) recently performed simulations using an LES approach at Re=6.0×10^6, employing a discretization with a total of 185 million grid nodes and an immersed boundary method for the blades and turbine structure. Through this methodology they could resolve the instantaneous flow field and predict the torque and power generated by the turbine (Kang et al., 2012).

In spite of the detailed information that these highly resolved simulations provide, they can become very intensive in terms of the use of computational resources when many turbines have to be considered. At intermediate spatial scales, simulations of multiple interacting turbines might require a parameterization to represent their effects, incorporating a momentum sink in the governing equations at the location of the MHK devices. For hydrokinetic turbines Miller and Schaefer (Miller & Schaefer, 2010) used a Reynolds-averaged approach to perform two-dimensional simulations of the flow past a turbine, introducing a force in the momentum equation to reproduce the flow patterns around it. Recently Turnock et al. (Turnock, Phillips, Banks, & Nichollos-Lee, 2011) carried out 3D URANS simulations with a commercial CFD software to reproduce the mean flow past a turbine, showing that quantitatively accurate results required at least 6 million grid nodes with a large number of them concentrated in the wake region. Regarding the numerical models of upstream obstacles designed to improve the efficiency of the devices, Gaden and Bibeau (Gaden & Bibeau, 2010b, 2010a) carried out numerical simulations with a URANS approach to evaluate quantitatively the effects of structures to enhance the power production. The use of actuator disks has also been extensively applied to wind turbines. Recent investigations have focused on the development of LES models to resolve the wakes behind turbine arrays, and establish their interactions with the terrain. Calaf, Meneveau, and Meyers (2010); Calaf, Parlange, and Meneveau (2011) quantified the vertical transport of momentum and kinetic energy in the atmospheric boundary layer using different sub-grid scale models, and determined the roughness effects produced by the turbines.

Numerical simulations of flows past MHK devices are particularly challenging since they usually take place in complex terrain and at high Reynolds numbers. The installation of multiple turbines and the variability induced by the interaction of the wakes require numerical models capable of capturing the rich dynamics of the large-scale coherent structures that control momentum and mass transport in the vicinity of the turbine array. As observed in flows past surface-mounted obstacles, URANS simulations can capture with good accuracy the mean flow, but they cannot yield insights into the instantaneous flow field and turbulence statistics in regions dominated by large-scale coherent vortical structures (Paik, Escauriaza, & Sotiropoulos, 2007; Escauriaza & Sotiropoulos, 2011c). Large-eddy simulations (LES), on the other hand, can reproduce in detail the dynamic structure of turbulent wakes in many complex situations (Krajnović, 2009), but for fully resolved LES with a large number of turbines in high Reynolds numbers, the grid resolution required to resolve the most important features of the flow and the need to specify time-dependent turbulent inflow boundary conditions might increase considerably the computational costs of the simulations. Ideally, when computing realistic flows past multiple MHK devices, numerical models should satisfy the following attributes: (1) Resolve the rich dynamics of the wakes to capture the instantaneous interactions produced by the turbulent coherent structures; (2) Deal with complex arbitrary bathymetries of the natural channels; and (3) Employ low-cost modeling techniques to incorporate the regions of interest with good resolution and multiple turbine arrangements. Recent studies of flows dominated by turbulent coherent structures that emerge from large-scale instabilities (Paik et al., 2007; Paik, Escauriaza, & Sotiropoulos, 2010; Escauriaza & Sotiropoulos, 2011c) have shown that hybrid URANS/LES turbulence models such as the detached-eddy simulation (DES) approach (Spalart et al., 1997; Spalart, 2009) can resolve essentially all turbulence scales produced by obstacles installed in channels or streams. Therefore, the unsteady flow fields that are obtained from these computations can constitute an ideal framework to study the flow past MHK devices and wake interactions using low computational resources.

In addition, the detailed information given by these 3D models can be utilized to study the regional impacts that turbine arrays have on larger areas of the coastal region. In two-dimensional (2D) and 3D regional models, the size of the discretization might vary from meters to kilometers, depending on the grid resolution and size of the domain. The correct description of the roughness effects to estimate the energy losses can be extracted by using spatial-averaging techniques or control-volume approximations (Nikora, McLean, et al., 2007). Additionally, the statistically converged flows can also provide a parameterization for one-dimensional models that are used to estimate the energy extraction from tidal channels connected to bays or basins (Blanchfield, Garrett, Wild, & Rowe, 2008; Blanchfield, Garrett, Rowe, & Wild, 2008; Polagye, Malte, Kawase, & Durran, 2008; Polagye & Malte, 2011). For a detailed description of the bibliography in the three scales of modelation look at the Appendix A

With the availability of new detailed experimental data of MHK turbine models or disks (Bahaj, Batten, & McCann, 2007; Batten, Bahaj, Molland, & Chaplin, 2007; Myers & Bahaj, 2010, 2012), the numerical methodologies can be validated and improved to apply them in realistic cases. In this investigation we seek to evaluate the performance of the DES approach (Escauriaza & Sotiropoulos, 2011c, 2011b, 2011a) using an actuator disk model (Burton, Sharpe, Jenkins, & Bossanyi, 2001; Calaf et al., 2010, 2011) to develop a flexible and inexpensive computational tool, with the purpose of simulating the unsteady flow past multiple devices at large Reynolds numbers in complex bathymetries. We apply our model to study the experimental configuration of Myers and Bahaj (2010, 2012), and resolve the instantaneous wake dynamics and time-averaged flow field, establishing a framework for future optimizations and turbine array design on specific sites. We also analyze the computed flow fields at the channel scale, averaging in time and space the hydrodynamic variables to estimate the global energy that is extracted from these particular flows (Myers & Bahaj, 2010, 2012). From this methodology we can relate quantitatively the instantaneous resolved flow that arises from our numerical simulations to the variables employed in regional scale models, accounting for the additional roughness generated by MHK devices.

The paper is organized as follows: In Chapter 2 we describe the computational model used in this work, including the governing equations, the turbulence model, and the disk parameterization that is employed in this investigation to represent the turbines coupled with the hydrodynamic model that is used to simulate the experiments of Myers and Bahaj (2010, 2012). Chapter 3 contains the results of the simulations for one and two actuator disks, we compare the mean flow in the wake and calculate the turbulence statistics, including the resolved turbulence kinetic energy (TKE), and probability distribution functions (pdfs) of turbulent velocity fluctuations. The analysis incorporates the study of 3D vortical structures that emerge in the wake, which are also captured by the model. In Chapter 4 we present the analysis of the large-scale effects of the disks by upscaling the roughness and energy losses using spatial and time averaging techniques, and in Chapter 5 we summarize the findings of the present study and outline topics for future research.

2. COMPUTATIONAL MODEL

In this section we present the governing equations for the flow field and the parameterization of the momentum sink generated by the disks. The method we employ to calculate the instantaneous flow fields has been discussed in great detail in a series of previous papers (Paik et al., 2007, 2010; Escauriaza & Sotiropoulos, 2011c, 2011b, 2011a). We provide here an overview of the main features of the model and the DES approach. For more specific details the reader is referred to the above cited papers. Details of the 3D modeling of computational fluid dynamics (CFD) can be found on appendix B.

2.1. Governing Equations of the Resolved Flow and Numerical Model

The governing equations for the resolved flow are the 3D unsteady Reynolds-averaged continuity and Navier-Stokes equations non-dimensionalized using the water depth H and the bulk velocity $\mathcal{U}$ as characteristic length and velocity scales, respectively. The equations are transformed to a generalized curvilinear system to compute the flow field in complex domains and to ensure a finer resolution in regions of interest and solid boundaries. The governing equations in vector format and in strong conservation form can be written as follows:

$$\Gamma \frac{\partial Q}{\partial t} + J \frac{\partial}{\partial \xi^j} \left(F^j - F_v^j \right) + f = 0 \tag{2.1}$$

where

$$\Gamma = \mathrm{diag}\,[0\;1\;1\;1]$$

$$Q = [P,\; u_1,\; u_2,\; u_3]^T$$

$$F^j = \frac{1}{J} \left[U^j, u_1 U^j + P\xi^j_{x_1}, u_2 U^j + P\xi^j_{x_2}, u_3 U^j + P\xi^j_{x_3} \right]^T$$

$$F_v^j = \frac{1}{J} \left(\frac{1}{Re} + \nu_t \right) \left[0, g^{mj} \frac{\partial u_1}{\partial \xi^m} + R_{m1}\xi^j_{x_m}, g^{mj} \frac{\partial u_2}{\partial \xi^m} + R_{m2}\xi^j_{x_m}, g^{mj} \frac{\partial u_3}{\partial \xi^m} + R_{m3}\xi^j_{x_m} \right]^T$$

In these equations $P = p + \frac{2}{3}k$, where k is the turbulence kinetic energy and p is the pressure divided by the density, u_i ($i = 1, 2, 3$) are the Cartesian velocity components, x_i

are the Cartesian coordinates, J is the Jacobian of the curvilinear coordinate transformation, $\xi^j_{x_i}$ are the metrics of the transformation, U^j are the contravariant velocity components $U^j = u_i \xi^i_{x_j}$, g^{ij} are the components of the contravariant metric tensor $g^{ij} = \xi^i_{x_k}\xi^j_{x_k}$, Re is the Reynolds number defined as $Re = \mathcal{U}H/\nu$, where ν is the kinematic viscosity of the fluid. The eddy viscosity is defined as ν_t, and the tensor R_{ij} is $R_{ij} = \frac{\partial u_i}{\partial \xi^k}\xi^k_{x_j}$.

The vector f on the left hand side of equation (2.1) can become a source or sink of momentum and it is employed to incorporate the effects of the actuator disks on the flow field. The non-dimensional Cartesian components of this vector f_{x_i} are calculated from the actuator disk model that is discussed in the following sections.

2.2. Turbulence Model

For the turbulence model we employ the DES approach (Spalart et al., 1997; Spalart, 2009), which is a hybrid URANS/LES formulation based on the one-equation eddy-viscosity model of Spalart-Allmaras (S-A) (Spalart & Allmaras, 1994). The model can be expressed in the curvilinear coordinate system as follows:

$$\frac{\partial \widetilde{\nu}}{\partial t} + J\frac{\partial}{\partial \xi^j}\left[F^j_t - F^j_{tv}\right] + J\, H_t = 0 \tag{2.2}$$

where

$$F^j_t = \frac{1}{J}\left[\left(U^j - U^j_0\right)\ \widetilde{\nu}\right]$$

$$F^j_{tv} = \frac{1}{J}\left[\frac{1}{\sigma}\left(\frac{1}{Re} + \widetilde{\nu}\right) g^{mj}\frac{\partial \widetilde{\nu}}{\partial \xi^m}\right]$$

$$H_t = \frac{1}{J}\left[-c_{b_1}\left(1 - f_{t_2}\right)\widetilde{S}\widetilde{\nu} + \left(c_{w_1}f_w - \frac{c_{b_1}}{\kappa^2}f_{t_2}\right)\left(\frac{\widetilde{\nu}}{d_w}\right)^2 - \frac{1}{\sigma}c_{b_2}g^{mj}\frac{\partial \widetilde{\nu}}{\partial \xi^m}\frac{\partial \widetilde{\nu}}{\partial \xi^m}\right]$$

The working variable $\tilde{\nu}$ in the S-A turbulence model has a direct relation to the eddy viscosity, ν_t, and the destruction term contains the length scale d_w, which is defined as the distance from solid walls. For a detailed explanation of the variables and functions that appear in the turbulence model equation (2.2) the reader is referred to (Paik et al., 2007).

The DES approach is such that the S-A turbulence model in equation (2.2) functions in URANS mode near solid boundaries while switches to perform the role of the sub-grid scale (SGS) model in the LES region away from the wall, where the grid density is sufficient to resolve the energetic scales of fluid motion (Spalart et al., 1997; Spalart, 2009). The modification to the S-A model to implement DES consists on replacing the distance to the nearest wall as the length-scale of the model by the following expression:

$$\widetilde{d} \equiv \min\left(d_w,\ C_{DES}\Delta\right) \tag{2.3}$$

where $\Delta \equiv \max\left(\Delta x,\ \Delta y,\ \Delta z\right)$, is the largest dimension of the grid cell and the model constant is set equal to its standard value $C_{DES} = 0.65$, which was calibrated for homogeneous turbulence (Shur, Spalart, Strelets, & Travin, 1999). By implementing this modification the DES model transitions from the URANS to LES mode depending on the local grid spacing. If the computational grid is constructed such that the wall-parallel grid spacing is of the order of the boundary layer thickness, the S-A URANS model is retained throughout the boundary layer. Far from the solid boundaries the model becomes a SGS eddy-viscosity equation. When the production balances the destruction term of the model the length scale in the LES region yields a Smagorinsky eddy-viscosity. Analogous to the classical LES formulation, the role of Δ is to allow the energy cascade down to a length scale proportional to the grid size, making a pseudo-Kolmogorov length-scale based on the eddy viscosity proportional to Δ.

2.3. Model of Turbines as Actuator Disks

In this investigation we use actuator disks to represent the effect of turbines on the flow through the momentum sink term f incorporated in the governing equations (2.1). This model is based on the simplifications initially developed for wind turbines (Burton et al., 2001) to represent the devices, and compute their effects in the flow hydrodynamics. A detailed description of the actuator disk model and its equations can be found on appendix C. Here we adopt a similar approach to the recent work by Calaf, Meneveau, and Meyers (2010); Calaf, Parlange, and Meneveau (2011). The averaged thrust force produced by the turbines is different from zero only at the location of the devices. The force per unit mass in equation (2.1), for the streamflow direction x, is therefore computed in each grid node within the area of the disk using the following expression,

$$f_x(i,j,k) = -\frac{1}{2} C_T V_d^2 \delta A_d \tag{2.4}$$

where C_T is the thrust coefficient, V_d the instantaneous disk-averaged flow velocity, and δA_d the proportion of the area of the disk represented by the node (i,j,k) in the computational mesh, considering the disk porosity. The model can also incorporate tangential forces in the y and z directions that account for the rotation of the turbine. In the simulations presented in this work, however, they are omitted as the disks are fixed in the experiments (Myers & Bahaj, 2010, 2012) and they only contribute horizontal momentum facing the bulk flow. In general, the magnitude of the thrust coefficient C_T for a MHK turbine is usually computed in terms of an induction factor that can be estimated from the geometry of the turbine, the number of blades and dimensions, and the blade pitch (Burton et al., 2001). Here we use the values of C_T reported by Myers and Bahaj (2010, 2012).

It is important to point out that the turbulence closure for URANS simulations or the subgrid scale (SGS) model of LES may require additional modifications, depending on the influence of the turbine on the unresolved scales of motion, and the contribution of the to force given by equation (2.4). In this case, however, there is a very limited effect of the subgrid scales due to the dimensions of the disks with respect to the grid size and channel, which produce large time scales compared to the unresolved fluctuations. SGS models could become important when turbine scales are small for the resolution of the numerical simulation, but in the conditions computed in this work they are much larger than the scales of the unresolved motions. As it will be shown in the following section, the wake dynamics is driven by large-scale coherent structures which are fully resolved by the DES model.The changes in the base code to include the actuator disk forces can be found on appendix D.

2.4. Test Case and Computational Details

We simulate the flow past porous disks representing MHK devices installed in a rectangular open channel. This configuration was studied experimentally by Myers and Bahaj (2010, 2012) who carried out flow measurements in the wake of the disks to determine the flow recovery as a function of the thrust produced by the devices and analyze the flow interaction in turbine arrays. The experiments were performed in a flume 21 m long by 1.35 m wide, with a water depth of $H = 0.3$ m. The mean velocity of the flow is equal to 0.25 m/s, which yields a Reynolds number of $Re = 75,000$ and a Froude number of $Fr = 0.14$ based on the flow depth H. Fig. 2.1 shows the experimental set-up with one and two disks in the laboratory channel (Myers & Bahaj, 2010, 2012).

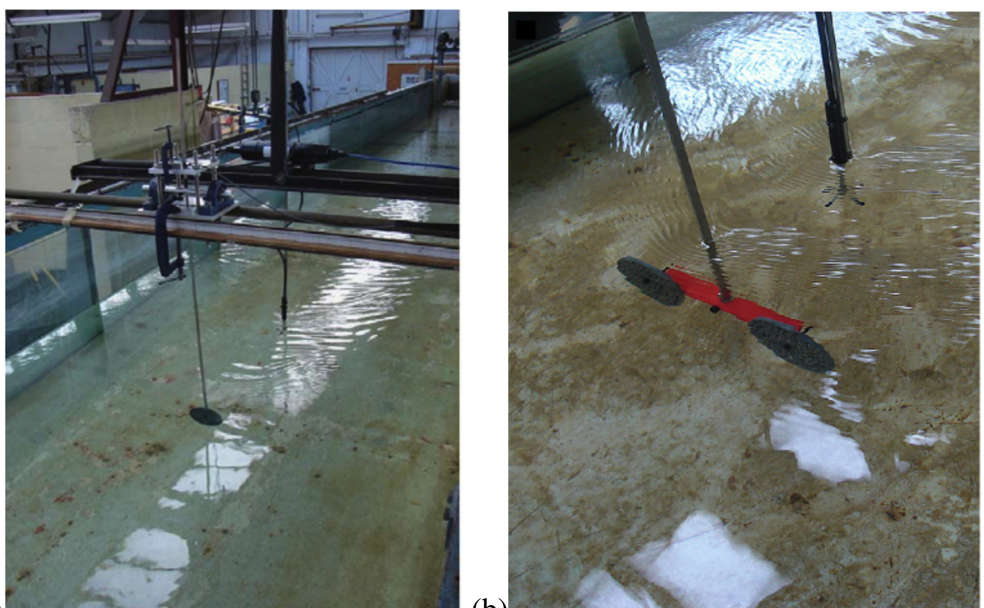

(a) (b)

FIGURE 2.1. Experimental set-up of the investigation carried out by Myers and Bahaj (2010, 2012). (a) Single disk configuration (Myers and Bahaj, 2010); and (b) Two-disk configuration (Myers Bahaj, 2012).

The actuator disks of diameter $D = 0.1$ m were located in a section of the flume which had already reached a fully-developed turbulent channel flow. The disks were mounted in a rig with a pivot to amplify the forces and measure the total thrust with good accuracy.

To vary the disk thrust, different porosities from 0.48 to 0.35 were tested using the same upstream flow conditions. Flow data was collected using Acoustic-Doppler velocimeters (ADV) with a sampling frequency of 50 Hz, considering a measurement area extending from $3D$ to $20D$ downstream, and vertically the instantaneous velocities were measured at a resolution of $0.1H$ (Myers & Bahaj, 2010, 2012).

The computational domain models a section of the experimental flume that is $16H$ long and the disks are placed at the center of the cross section, as shown in Fig. 2.2. For all the simulations presented in this investigation we use a grid with a total of 4.1 million nodes, which constitutes a fairly coarse computational mesh requiring reduced computational resources for a wake-resolving 3D simulation.

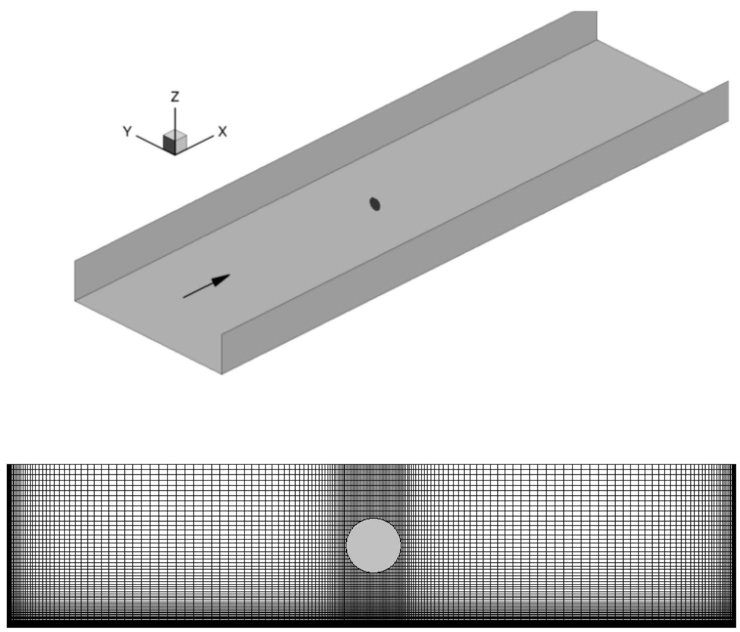

(a)

(b)

FIGURE 2.2. (a) Computational domain showing the location and size of the single disk simulations; and (b) Cross-section of the channel, depicting the grid at the location of the disk.

The governing equations of the flow are discretized on a non-staggered computational grid using second-order accurate finite-volume discretizations for all the spatial derivatives. Central differencing is employed for the viscous fluxes, pressure gradients and source terms, and upwind QUICK scheme is used for all the convective terms. A third-order fourth-difference artificial dissipation is added to eliminate the odd-even decoupling of the pressure field due to the non-staggered mesh layout (Sotiropoulos & Abdallah, 1992).

The time integration is carried out by adopting a dual (or pseudo) time-stepping artificial compressibility (AC) method. The discretized equations are then integrated, advancing the solution in pseudo-time using a pressure-based implicit preconditioner (Sotiropoulos & Constantinescu, 1997) enhanced with local time-stepping and V-cycle multigrid acceleration. The physical time derivative is discretized with a three-point-backward, second order accurate, Euler implicit temporal-integration scheme. The equations for the turbulence model are integrated with second order schemes, advancing the solution in pseudo-time using the standard alternate direction implicit (ADI) scheme. All the simulations are carried out using a non-dimensional physical time step of $\Delta t = 0.01$. This method has been shown to be effective in unsteady simulations of turbulent flows with the DES approach, and has already been described extensively in our previous work (Escauriaza & Sotiropoulos, 2011c, 2011b).

At the inflow of the computational domain we specify fully-developed, turbulent channel flow, obtained from a separate RANS simulation using the S-A turbulence model at the corresponding Reynolds number with the entire length of the experimental flume. At the outflow boundary we apply non-reflecting characteristic boundary conditions for incompressible flows (Paik, Sotiropoulos, & Sale, 2005). The computational mesh and the walls is fine enough to resolve the viscous sub-layer. For all meshes used in this work the first grid node off of the solid walls is always located at $z^+ \leq 0.5$, and no-slip boundary conditions are applied at these solid surfaces. The free surface is approximated as a flat and rigid slip wall and symmetry boundary conditions are applied for the resolved flow variables. This treatment is valid under the assumption that the gravity force is strong enough to suppress vertical free-surface fluctuations, which is consistent with the small Froude number of the experiments ($Fr = 0.14$). No modifications are introduced into the turbulence model near the free surface.

3. FLOW PAST ACTUATOR DISK IN A RECTANGULAR CHANNEL

In this Chapter we present the results of the simulations for one disk at different vertical positions in the channel, corresponding to $0.33H$, $0.5H$, $0.66H$ and $0.75H$ (Myers & Bahaj, 2010), and the flow past two parallel disks separated horizontally by $0.5D$, $1.0D$, and $1.5D$ at a depth of $0.5H$ (Myers & Bahaj, 2012). The time-averaged flow fields computed with the DES turbulence model and the numerical methods described in Chapter 2 above are compared with the experimental measurements. We discuss the recovery of the streamwise velocity in the wake and the turbulence statistics in the same planes reported in the experiments. Subsequently, we examine the three-dimensional flow fields discussing the structure of the instantaneous large scale vortices in the wakes, showing that the model can be employed as a tool to probe deeper into the physics of the flow past MHK devices.

3.1. Mean Flow and Resolved Turbulence Kinetic Energy

Myers and Bahaj (2010, 2012) measured the flow behind the disks and reported the mean streamwise velocity at the vertical symmetry plane across the channel. To describe the wake recovery behind the disks, they studied the flow field in terms of a non-dimensional velocity deficit, defined as the relative difference between the time-averaged streamwise velocity and the free-stream velocity by the following expression,

$$\mathcal{U}_{def} = 1 - \frac{\overline{U}}{\mathcal{U}_0} \tag{3.1}$$

where $\mathcal{U}_{def}$ is the non-dimensional velocity deficit, $\overline{U}$ is the time-averaged streamwise velocity at every point in space, and $\mathcal{U}_0$ is the free stream velocity of the channel flow in the experiment.

For the case of a single disk, in Fig. 3.1 we show the comparison of the velocity deficit for the center of the disk located at a depth of $0.5H$, for three different thrust coefficients C_T equal to 0.61, 0.86, and 0.94. By using the same contour scale for the measurements and computational results, we observe a good quantitative agreement not only in the magnitude of $\mathcal{U}_{def}$, but also in the spatial distribution of the wake. The calculated velocity deficits seem to be slightly larger closer to the disks compared to the experiments, and their longitudinal size has a good agreement to the observed flow fields. As reported by Myers and Bahaj (2010), stronger initial deficits occur in disks with larger values of C_T and the numerical simulations also show that for a distance beyond $10D$ downstream from the disk the wakes characterized by $\mathcal{U}_{def}$ are very similar at the center plane of the channel, with low values of the velocity deficit.

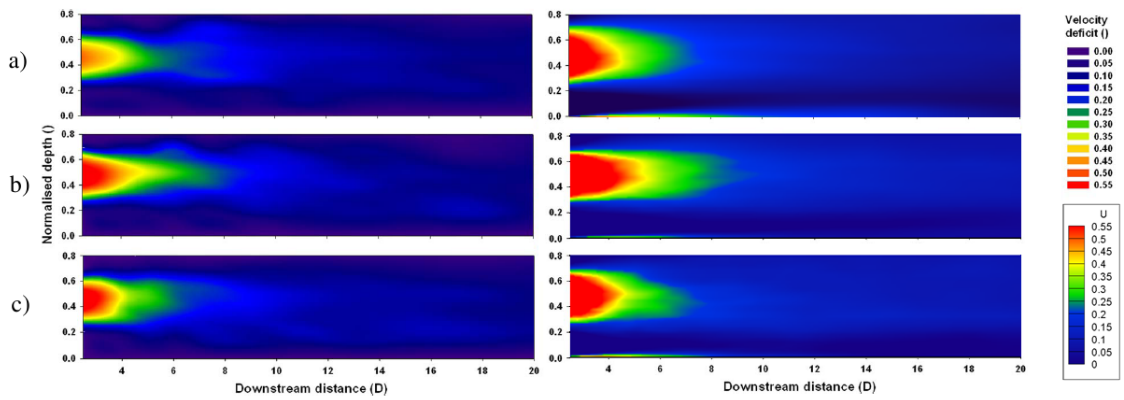

FIGURE 3.1. Comparison of the velocity deficit $\mathcal{U}_{def}$ at the central vertical plane of the rectangular channel. The left pane shows the wake measured by Myers and Bahaj (2010) and the right pane shows the computation results from the DES approach with thrust coefficients C_T equal to a) 0.61, b) 0.86 and c) 0.94.

The centerline variation of $\mathcal{U}_{def}$ plotted in Fig. 3.2 allows for a better comparison of the mean flow in the wake between the experiments and simulations. The decrease on the velocity deficit shows that the numerical simulations capture the rate at which the time-average velocity recovers behind the disk and the similarities of all three flows for longer distances (Myers & Bahaj, 2010). From this plot we compute the differences between the simulation and the experimental measurements. The data shows that for $C_T = 0.94$ the average error is 5%. For $C_T = 0.86$, on the other hand, the rate of decrease in the velocity deficit is practically identical to the experiment, and for $C_T = 0.61$, the average error is around 6%. The initial errors might be produced by the homogeneous porosity that is assigned to the model, compared to the heterogeneous distribution of the disks in the experiment. It is also important to note that the discrepancies might also arise due to the difficulty on measuring these complex flow fields. Errors due to resolution of vertical and horizontal measurements reported above can produce differences on the spatial distribution of the velocity deficit contours, or decrease the total magnitude of $\mathcal{U}_{def}$.

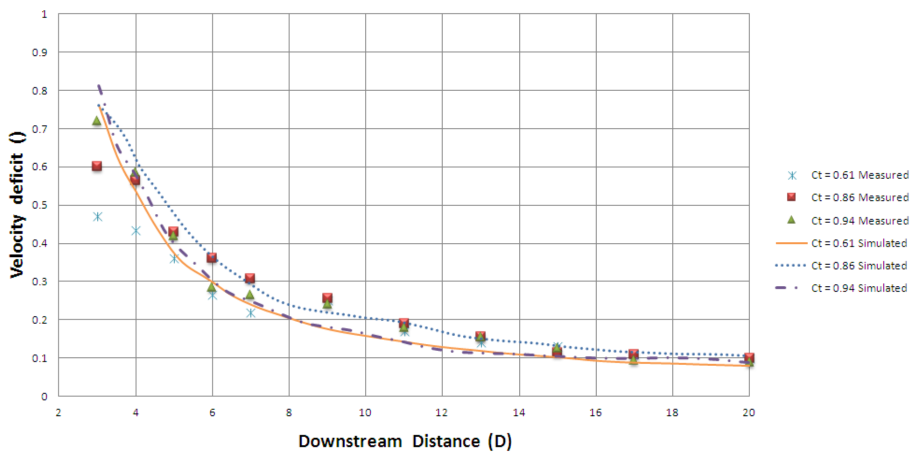

FIGURE 3.2. Plots of the centerline velocity deficit from the model with the values of the measurements (Myers Bahaj, 2010) with C_T values of 0.61, 0.86, 0.94.

To evaluate the operation of MHK turbines at different depths in the water column, Myers and Bahaj (2010) carried out experiments at different depths to represent the operation of the turbine rotor closer to the free surface or to the channel bed. Fig. 3.3 shows good agreement between the experimental and computed wakes in these three cases, using the same disk centered at a water depth of a) 0.75, b) 0.66 and c) 0.33, the depths are non-dimensionalized using H, and $C_T = 0.86$.

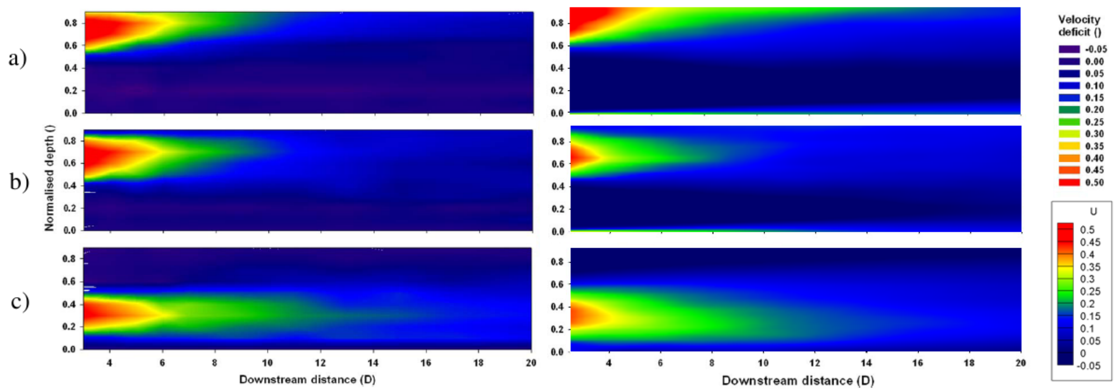

FIGURE 3.3. Comparison of the velocity deficit $\mathcal{U}_{def}$ at the central vertical plane of the rectangular channel. The left pane shows the wake measured by Myers and Bahaj (2010) and the right pane shows the computation results from the DES approach for the actuator disk located at water depths of a) 0.75, b) 0.66 and c) 0.33, considering a thrust coefficient of $C_T = 0.86$.

Myers and Bahaj (2012) also performed experiments with multiple disks to study the wake behind MHK devices with two rotors, varying the lateral separation of the disks from $0.5D$ to $1.5D$. The flexibility of the model also allows the inclusion of multiple disks, as shown in Fig. 3.4, obtaining good agreement of the computed velocity deficit compared to the experiments.

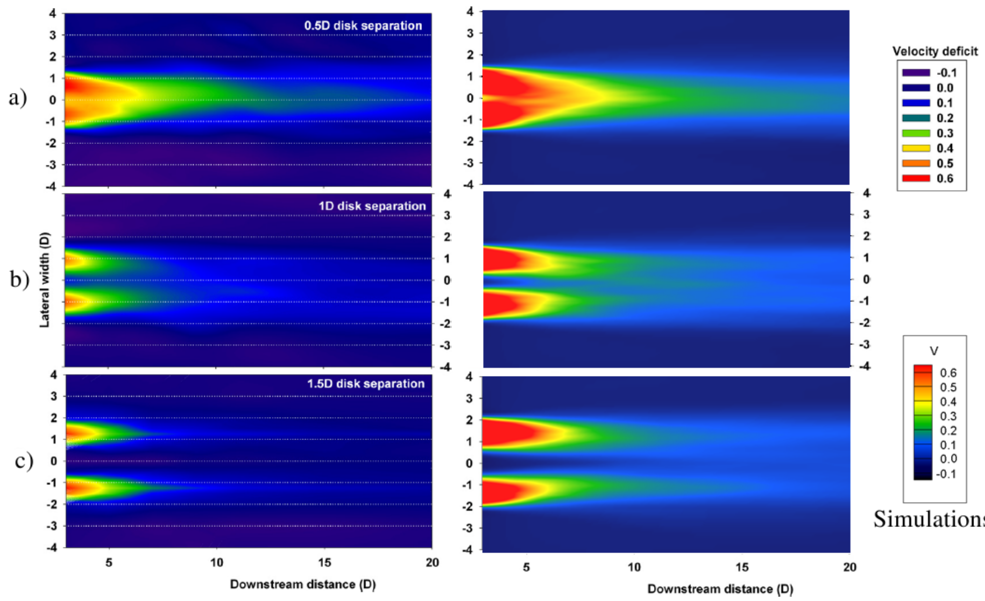

FIGURE 3.4. Comparison of the velocity deficit $\mathcal{U}_{def}$ at the central vertical plane of the rectangular channel. The left pane shows the wake measured by Myers and Bahaj (2012) and the right pane shows the computation results from the DES approach for two actuator disks with separations from $0.5D$ to $1.5D$, considering a thrust coefficient of $C_T = 0.91$ and $C_T = 0.94$ respectively.

From the simulations we can also explore the turbulence statistics of the wakes in the entire computational domain. As an example of our results, and for the sake of clarity, we only plot in Fig. 3.5 the contours of resolved turbulence kinetic energy (TKE) in a vertical plane behind the disk located at $0.33H$ with $C_T = 0.86$. The results show the TKE peaks at the disk edges with the effect of the wall and the interaction with the bed. Although they are not shown herein, similar results were obtained for all the cases we computed in the present investigation.

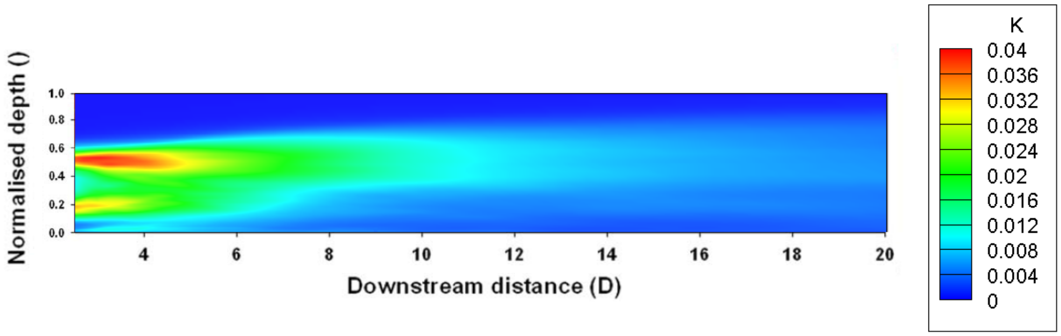

FIGURE 3.5. Non-dimensionalized resolved TKE in a vertical plane behind the disk at $0.33H$ and $C_T = 0.86$ (Myers Bahaj, 2012).

To summarize, the results presented in this section collectively suggest that our simulations capture the most important features of the time-averaged flow as observed in experiments.The TKE contours show an increase of the magnitude of velocity fluctuations at the disk edges and also the interaction with the wall. In the next section we analyze the unsteady features of the flow that produce these turbulence statistics and discuss the mechanisms that characterize the instantaneous wake behind the disks. In appendix E, the validation of the model is shown and also the results are commented in detail.

3.2. Instantaneous 3D Flow Field in the Wake

The time-averaged statistics depend on the instantaneous flow patterns that are formed in the wake of the disks. Here we describe the unsteady 3D flow field behind the devices, which characterizes the mean flow observations reported in the experiments. We extract time-series of velocity fluctuations at specific points in the wake and plot the probability distribution functions (pdf) in figure 3.6, for a disk located at $0.5H$, and $C_T = 0.61$. The velocity time series are extracted at six different points along the axis of the disk in the downstream direction. The histograms in semi-log scale show that the distribution of unsteady velocity fluctuations are very similar to a Gaussian distribution. Power spectral densities of these time series (shown on appendix F), reveal that the instantaneous wake flow is dominated by the low-frequency unsteadiness with dominant frequencies of $f = 0.73$

Hz and $f = 0.27$ Hz, showing a quasi-periodic dynamics driven by large-scale coherent vortices

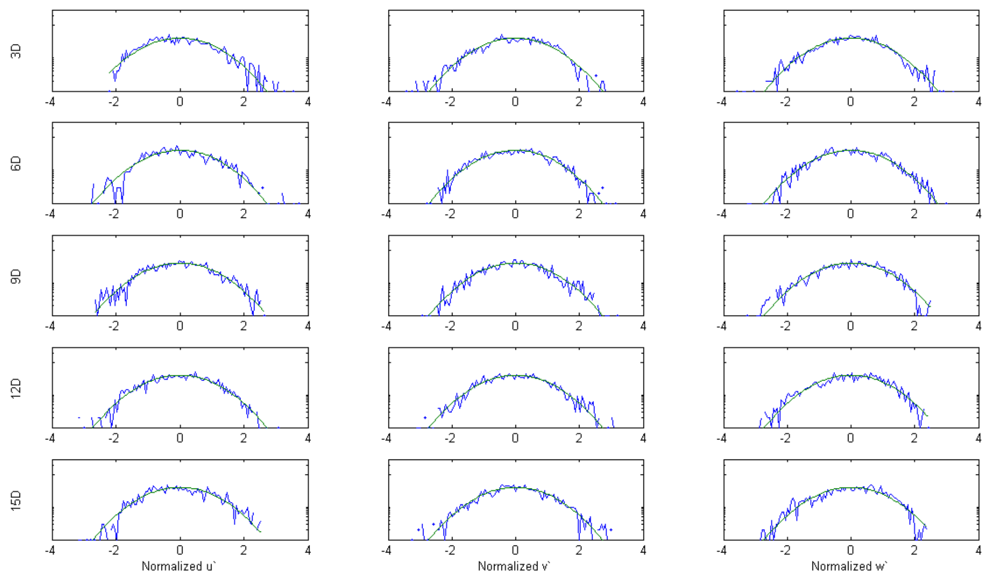

FIGURE 3.6. Histograms of non-dimensional velocity fluctuations at the centerline, and horizontal distances from the disk of $3D$, $6D$, $9D$, $12D$, $15D$ and $18D$, respectively. The disk is located at $0.5H$ and $C_T = 0.61$. The continuous line corresponds to a Gaussian distribution.

To elucidate the three-dimensional phenomena that cause these features of the turbulence fluctuations in the wake, we visualize the 3D coherent dynamics of the flow using the so-called q-criterion (Hunt, Wray, & Moin, 1988), defined as:

$$q = \frac{1}{2}\left(\Omega_{ij}\Omega_{ij} - S_{ij}S_{ij}\right) \tag{3.2}$$

where Ω_{ij} and S_{ij} denote the antisymmetric and symmetric parts of the velocity gradient tensor respectively. According to Hunt et al. (Hunt et al., 1988), we can identify vortical structures in regions where $q > 0$, where the local rotation rate dominates the strain rate.

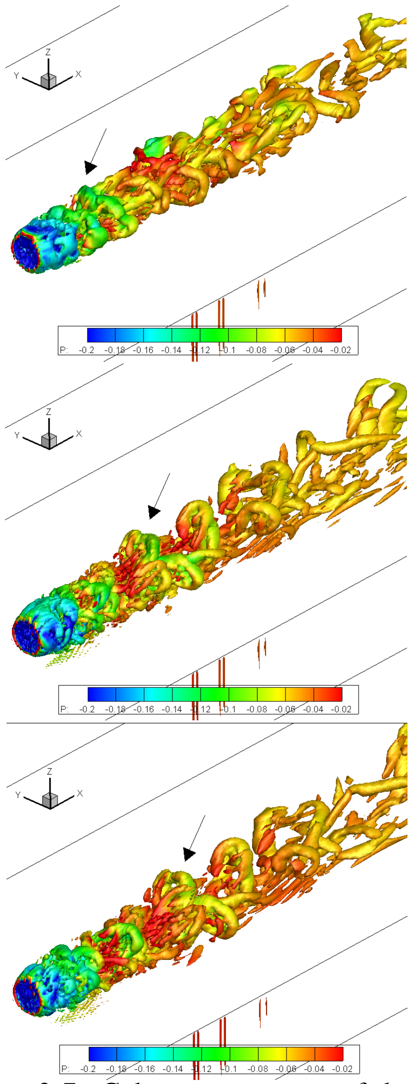

FIGURE 3.7. Coherent structures of the wake for a disk is located at $0.5H$ and $C_T = 0.94$. Instantaneous images are separated by 0.6 s and the arrow marks the evolution of an arch vortex growing from the disk edges.

Figure 3.7 shows a series of snapshots of the coherent structures of the wake visualized with the q-criterion for the case with a thrust coefficient $C_T = 0.94$ with the disk located at $0.5H$. The q-isosurfaces are colored by pressure contours, showing the low pressure zone behind the disk and the unsteady pressure variations along the wake. As depicted in the sequence plotted in figure 3.7, the instantaneous flow field consist of multiple large-scale vortical structures that emerge from the disk edges, interacting and growing in the downstream direction. The asymmetric and dynamically-rich turbulent wake generated by the disks is characterized by the so-called half-arch vortices that form a von Kármán street-like flow downstream. These organized vortices are seen to emerge in the flow past bluff bodies with sharp edges in a large number of situations (Krajnović, 2009). It is important to point out, however, that in our simulations we can capture this complex dynamics of the wakes even though we are not representing physically the disks in the computational domain, but as a force incorporated in the governing equations of the flow. The arrow in each pane of figure 3.7, identifies a single arch vortex in the wake as it evolves in time, and the instantaneous images are separated by 0.6 s.

Similar results are obtained for the cases with two disks as depicted in figure 3.8. The wakes are characterized by large-scale coherent structures in the form of arch vortices that interact in the downstream direction. The instantaneous q-isosurfaces for the two-disk array, with $C_T = 0.94$ and separated by one diameter, also show the low-pressure zone between the disks produced by the narrowing of the flow.

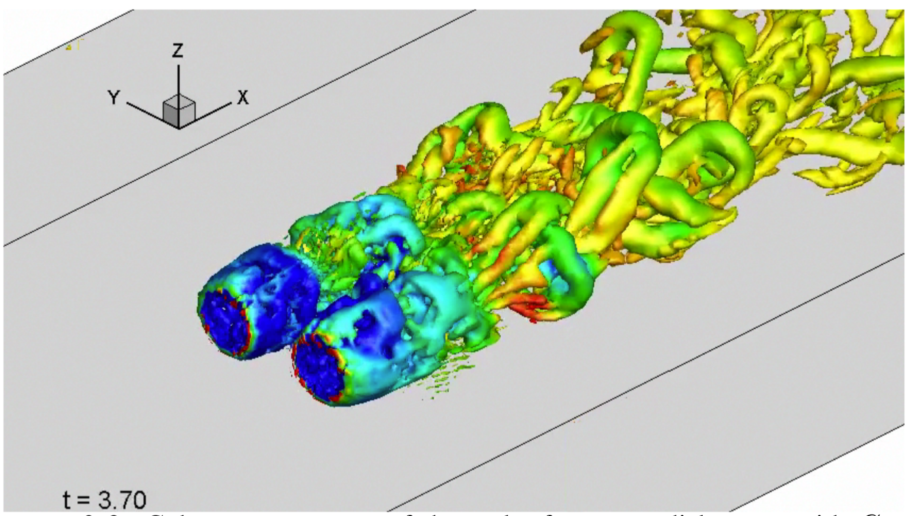

FIGURE 3.8. Coherent structures of the wake for a two-disk array with $C_T = 0.94$ and separated by one diameter. The q-isosurfaces colored by the pressure magnitude show the instantaneous wake interaction.

4. SPATIAL AVERAGING AND UPSCALING

An important application of the model developed in this investigation is also the use of the 3D simulations to estimate the effects of the turbines at larger scales. Regional models of a large area of the coast usually require information of the stresses generated by the MHK turbine array, which in this case can be obtained from the results of the DES computations.

Using this information the regional models can be employed to evaluate the effect of the turbines on the tidal flow, and to understand better the environmental impacts that can be potentially produced due to the changes on the hydrodynamic conditions. Spatial averaging techniques can be applied to the 3D simulations with actuator disks to estimate the stresses in the entire section of the channel, including the additional roughness generated by the MHK devices.

Simplified 1D models that are used to estimate the energy that can be harnessed from a tidal channel (Blanchfield, Garrett, Wild, & Rowe, 2008; Blanchfield, Garrett, Rowe, & Wild, 2008; Polagye et al., 2008) or a network of channels and basins (Polagye & Malte, 2011) employ the one-dimensional shallow-water equations and consider the roughness based on expressions developed for uniform flow such as Manning's equation. If we adopt a control volume approach to compute the time and spatial averaged momentum difference produced by the channel walls and the disks, the momentum difference between the inlet and the outlet of the channel is always less than 10%. For instance, the sum of the momentum produced by the wall shear stress and one disk at $0.5H$ and $C_T = 0.86$ is computed from momentum difference and the total pressure between the inlet and the outlet of the channel. The combined effect in this case is a decrease of 4.4% of the total momentum that enters the computational domain.

The most appropriate methodology to perform the upscaling of the 3D model results to larger scale models is to employ spatial-averaging techniques that can parameterize the effects of the turbines on regional flows. The momentum equations can be averaged in time and space to provide a representation of the entire channel roughness (Nikora, McLean, et al., 2007; Nikora, McEwan, et al., 2007), in terms of a SGS stress tensor that represents the aggregated effect of all the processes that occur along the channel.

If the spatial averaged equations were applied to the entire computational domain, assuming that the channel would comprise an element of a discretization in a larger scale model, the form-induced stresses generated by the dynamic processes within the channel would arise as a symmetrical tensor with spatial correlations that would be used to parameterize the effect of the turbines at larger scales. To obtain this stress tensor, the hydrodynamic variables in the URANS equations are separated as the sum of a spatial average and a spatial fluctuation as $U_i = \langle U_i \rangle + \widetilde{u}_i$. By applying this decomposition to the URANS model, the equations can incorporate the statistical effect of the SGS fluctuations on the mean flow through a tensor of the form $\langle \widetilde{u}_i \widetilde{u}_j \rangle$.

To quantify the effects of a disk in a channel, we compare the tensor of spatial velocity correlations in the computational domain between a fully-developed channel flow and the same channel with an actuator disk located at $0.5H$ and $C_T = 0.86$, which yield the following values,

$$\langle \widetilde{u}_i \widetilde{u}_j \rangle_{\text{no disk}} = \begin{bmatrix} 4.28 \times 10^{-9} & 7.96 \times 10^{-11} & -5.28 \times 10^{-10} \\ 7.96 \times 10^{-11} & 1.21 \times 10^{-9} & 5.45 \times 10^{-11} \\ -5.28 \times 10^{-10} & 5.45 \times 10^{-11} & 2.78 \times 10^{-10} \end{bmatrix} \tag{4.1}$$

$$\langle \widetilde{u}_i \widetilde{u}_j \rangle_{\text{disk}} = \begin{bmatrix} 1.42 \times 10^{-4} & -2.00 \times 10^{-7} & 5.28 \times 10^{-6} \\ -2.00 \times 10^{-7} & 4.28 \times 10^{-5} & 3.15 \times 10^{-7} \\ 5.28 \times 10^{-6} & 3.15 \times 10^{-7} & 4.37 \times 10^{-5} \end{bmatrix} \tag{4.2}$$

The global effect of the disks using this approach can be recognized from the magnitude of the stresses. The anisotropic and heterogeneous flow within the channel increases the different components of the tensor due to the presence of the disk. It is important to point out that the most significant change occur on the normal stresses which changes five orders of magnitude when the disk is present, due to the effect of the wake on the flow field. This method will be employed in future investigations to upscale the turbine effects in real flows that will take place in complex bathymetries with turbine arrays. A further explanation of the upscaling equations and the calculation of the tensor of spatial velocities correlations can be found on Appendix G.

5. CONCLUSIONS AND FUTURE WORK

The model developed in this investigation can reproduce with quantitative agreement all the features measured for channel flows with actuator disks in the recent experiments of Myers and Bahaj (2010, 2012). The numerical solutions and comparisons with experimental data reported in this work further confirm the reliability of the DES model to simulate turbulent flows with actuator disks representing MHK devices. We can resolve the mean flow velocity deficit and also the turbulence statistics of the wake at high Reynolds numbers for one and two disks, and employing a discretization of 4.1 million grid nodes. The errors documented in regions very close to the disk are likely due to the resolution of the experimental data and the homogeneous disk porosity considered in the model.

The 3D dynamics of the flow field shows that the turbulent wake is characterized by the asymmetric formation of arch vortices that emerge from the disk edges and interact downstream producing a quasi-periodic dynamics of the velocity fluctuations in the wake. These mechanisms are essentially identical to what has been reported in the literature for similar flows, even though in our simulations we resolve these dynamic features by only adding a momentum sink in the governing equations.

The numerical model can also be employed to estimate subgrid stresses in regional models, upscaling the roughness produced by the turbine array using spatial averaging techniques. The calculation of the stress tensor obtained by averaging the entire channel in one of the cases computed in this investigation, shows a significant increase on the normal turbulence stresses produced by a disk, which might become important in large scale models when the effects of the MHK devices are parameterized for computing regional flows near the coast.

In summary, the important conclusion that emerges collectively from the present simulations is the good predictive capabilities of the numerical model, which can yield the time-averaged and instantaneous dynamics of flows past actuator disks in complex flows, at high Reynolds number, using low computational resources, and with the potential of incorporating the bathymetry natural aquatic environments. Future work will focus on implementing a dynamic feedback between regional models and our 3D model, considering multiple disks in complex bathymetry. We will also utilize the model to study further the effects of the installation of MHK devices such as sediment transport and scour, environmental impacts due to the local hydrodynamics, and also to design laboratory experiments that will be carried out at the Hydraulic Laboratory of the Pontificia Universidad Católica de Chile. We expect this model to become an important tool in the design of turbine arrays in the Chacao channel and in other similar sites.

References

(2010). In B. Polagye, B. van Cleve, A. Copping, & K. Kirkendall (Eds.), *Environmental effects of tidal energy development* (p. 181). U.S. Dept. Commerce, NOAA Tech. Memo. F/SPO-116.

Antheaume, S., Maître, T., & Achard, J.-L. (2008). Hydraulic darrieus turbines efficiency for free fluid flow conditions versus power farms conditions. *Renew. Energ.*, *33*, 2186-2198.

Bahaj, A., Batten, W., & McCann, G. (2007). Experimental verifications of numerical predictions for the hydrodynamic performance of horizontal axis marine current turbine. *Renew. Energ.*, *32*, 2479-2490.

Barroso, L. A., Rudnick, H., Sensfuss, F., & Linares, P. (2010). The green effect. *IEEE Power Energy Mag.*, *8*, 22-35.

Batten, W., Bahaj, A., Molland, A., & Chaplin, J. (2007). Experimentally validated numerical method for the hydrodynamic design of horizontal axis tidal turbines. *Ocean Eng.*, *34*, 1013-1020.

Blanchfield, J., Garrett, C., Rowe, A., & Wild, P. (2008). Tidal stream power resource assessment formasset sound,haida gwaii. *P. I. Mech. Eng. A-J. Pow.*, *222 (5)*, 485-492.

Blanchfield, J., Garrett, C., Wild, P., & Rowe, A. (2008). The extractable power froma channel linking a bay to the open ocean. *P. I. Mech. Eng. A-J. Pow.*, *222 (A3)*, 289-297.

Bryden, I. G., & Couch, S. J. (2007). How much energy can be extracted from moving water with a free surface: A question of importance in the field of tidal current energy? *Renew. Energ.*, *32*, 1961-1966.

Burton, T., Sharpe, D., Jenkins, N., & Bossanyi, E. (2001). *Wind energy handbook*. John Wiley & Sons, Ltd.

Calaf, M., Meneveau, C., & Meyers, J. (2010). Large eddy simulation study of fully developed wind-turbine array boundary layers. *Phys. Fluids*, *22*, 015110.

Calaf, M., Parlange, M. B., & Meneveau, C. (2011). Large eddy simulation study of scalar transport in fully developed wind-turbine array boundary layers. *Phys. Fluids*, *23*, 126603.

Escauriaza, C., & Sotiropoulos, F. (2011a). Initial stages of erosion and bed form development in a turbulent flow around a cylindrical pier. *J. Geophys. Res.*, *116*, F03007.

Escauriaza, C., & Sotiropoulos, F. (2011b). Lagrangian model of bed-load transport in turbulent junction flows. *J. Fluid Mech.*, *666*, 36-76.

Escauriaza, C., & Sotiropoulos, F. (2011c). Reynolds number effects on the coherent dynamics of the turbulent horseshoe vortex system. *Flow Turbul. Combust.*, *86*, 231-262.

Gaden, D., & Bibeau, E. (2010a). A numerical investigation into the effect of diffusers on the performance of hydro kinetic turbines using a validated momentum source turbine model. *Renew. Energ.*, *35*, 1152-1158.

Gaden, D., & Bibeau, E. (2010b). A numerical investigation into upstream boundary-layer interruption and its potential benefits for river and ocean kinetic hydropower. *Renew. Energ.*, *35*, 2270-2278.

Garrad-Hassan. (n.d.). *Preliminary site selection-chilean marine energy resources.* (http://www.cne.cl/cnewww/export/sites/default/05_Public_Estudios/descargas/estudios/texto10.pdf)

Garrett, C., & Cummins, P. (2008). Limits to tidal current power. *Renew. Energ.*, *33*, 2485-2490.

Gray, W. G. (1975). A derivation of the equation for multi-phase transport. *Chem. Eng. Sci.*, *30*, 229-233.

Güney, M. S., & Kaygusuz, K. (2010). Hydrokinetic energy conversion systems: A technology status review. *Renew. Sustain. Energ. Rev.*, *14*, 2996-3004.

Hunt, J. C. R., Wray, A. A., & Moin, P. (1988). Eddies, stream, and convergence zones in turbulent flows. In *Proceedings of the summer program.* Center for Turbulence Research, NASA Ames/Stanford Univ., pages 193-208.

Jameson, A., , Schmidt, W., & Turkel, E. (1981). Numerical solution of the euler equations by finite volume methods using runge-kutta time-stepping schemes. *AIAA Paper*, *81*, 1259.

Kang, S., Borazjani, I., Colby, J. A., & Sotiropoulos, F. (2012). Numerical simulation of 3D flow past a real-life marine hydrokinetic turbine. *Adv. Water Resour.*, *39*, 33-43.

Khan, J., Bhuyan, G., Moshref, A., Morison, K., Pease, J. H., & Gurney, J. (2008). Ocean wave and tidal current conversion technologies and their interaction with electrical networks. In *Power and Energy Society General Meeting - Conversion and Delivery of Electrical Energy in the 21st Century, IEEE* (p. 1-8).

Krajnović, S. (2009). Large-eddy simulation of flows around ground vehicles and other bluff bodies. *Phil. Trans. R. Soc. A*, *367*, 2917-2930.

Miller, V. B., & Schaefer, L. A. (2010). Dynamic modeling of hydrokinetic energy extraction. *J. Fluids Eng.*, *132*, 091102.

Myers, L., & Bahaj, A. (2006). Power ouput performance characteristics of a horizontal axis marine current turbine. *Renew. Energ.*, *31*, 197-208.

Myers, L., & Bahaj, A. (2010). Experimental analysis of the flow field around horizontal axis tidal turbines by use of scale mesh disk rotor simulators. *Ocean Eng.*, *37*, 218-227.

Myers, L., & Bahaj, A. (2012). An experimental investigation simulating flow effects in first generation marine current energy converter arrays. *Renew. Energ.*, *37*, 28-36.

Nikora, V., McEwan, I., McLean, S., Coleman, S., Pokrajac, D., & Walters, R. (2007). Double-averaging concept for rough-bed open-channel and overland flows: Theoretical background. *J. Hydraul. Eng.*, *133(8)*, 873-883.

Nikora, V., McLean, S., Coleman, S., Pokrajac, D., McEwan, I., Campbell, L., et al. (2007). Double-averaging concept for rough-bed open-channel and overland flows: Applications. *J. Hydraul. Eng.*, *133(8)*, 884-895.

Paik, J., Escauriaza, C., & Sotiropoulos, F. (2007). On the bimodal dynamics of the turbulent horseshoe vortex system in a wing-body junction. *Phys. Fluids*, *19*, 045107.

Paik, J., Escauriaza, C., & Sotiropoulos, F. (2010). Coherent structure dynamics in turbulent flows past in-stream structures: Some insights gained via numerical simulation. *J. Hydraul. Eng.*, *136*, 981-993.

Paik, J., Sotiropoulos, F., & Sale, M. J. (2005). Numerical simulation of swirling flow in complex hydroturbine draft tube using unsteady statistical turbulence models. *J. Hydraul. Eng.*, *131*, 441-456.

Polagye, B., & Malte, P. (2011). Far-field dynamics of tidal energy extraction in channel networks. *Renew. Energ.*, *36*, 222-234.

Polagye, B., Malte, P., Kawase, M., & Durran, D. (2008). Effect of large-scale kinetic power extraction on time-dependent estuaries. *P. I. Mech. Eng. A-J. Pow.*, *222(A5)*, 471-484.

Pope, S. B. (2000). *Turbulent flows*. Cambridge University Press.

Richardson, L. F. (1922). *Weather prediction by numerical process*. Cambridge University Press.

Sagaut, P. (2006). *Large eddy simulation for incompressible flows*. Third Edition, Springer, New York.

Sezer-Uzol, N., & Long, L. N. (2006). 3-D time-accurate CFD simulations of wind turbine rotor flow fields. *AIAA Paper*, *2006-394*, 1-23.

Shur, M., Spalart, P. R., Strelets, M., & Travin, A. (1999). Detached-eddy simulation of an airfoil at high angle of attack. In W. Rodi & D. Laurence (Eds.), *Turbulent shear flows* (p. 669-678). Elsevier Science, Amsterdam.

Sotiropoulos, F., & Abdallah, S. (1992). A primitive variable method for the solution of 3D, incompressible, viscous flows. *J. Comput. Phys.*, *103*, 336-349.

Sotiropoulos, F., & Constantinescu, G. (1997). Pressure-based residual smoothing operators for multistage pseudocompressibility algorithms. *J. Comput. Phys.*, *133*, 129-145.

Spalart, P. R. (2009). Detached-eddy simulation. *Annu. Rev. Fluid Mech.*, *41*, 181-202.

Spalart, P. R., & Allmaras, S. R. (1994). A one-equation turbulence model for aerodynamic flows. *Rech. Aerosp.*, *1*, 5-21.

Spalart, P. R., Jou, W. H., Strelets, M., & Allmaras, S. R. (1997). Comments on the feasibility of LES for wings and on a hybrid RANS/LES approach. In C. Liu & Z. Liu (Eds.), *Advances in DNS/LES.* Greyden Press, Columbus OH.

Turnock, S., Phillips, A. B., Banks, J., & Nichollos-Lee, R. (2011). Modelling tidal current turbine wakes using a coupled RANS-BEMT approach as a tool for analysing power capture of arrays of turbines. *Ocean Eng.*, *38*, 1300-1307.

Vennell, R. (2010). Tuning turbine in a tidal channel. *J. Fluid Mech.*, *663*, 253-267.

Wilcox, D. C. (1994). *Turbulence modeling for CFD*. California: DCW Industries.

Young, Y., ley, M., & Yeung, R. (2011). An insight into the separate flow and stall delay for hawt. *Renew. Energ.*, *36*, 69-76.

Yu, G., Shen, X., Zhu, X., & Du, Z. (2010). Three-dimensional numerical modeling of the transient fluid-structural interaction response of tidal turbines. *J. Offshore Mech. Arct.*, *132*, 011101-1.

Zahle, F., & Sørensen, N. N. (2011). Characterization of the unsteady flow in the nacelle region of a modern wind turbine. *Wind Energy*, *14*, 271-283.

Zanette, J., Imbault, D., & Tourabi, A. (2010). A design methodology for cross flow water turbines. *Renew. Energ.*, *35*, 997-1009.

Zikanov, O. (2010). *Essential computational fluid dynamics*. Hoboken, New Jersey: John Wiley & Sons, Inc.

APPENDICES

APPENDIX A. SCALES OF MODELATION

Models for studying flows around turbine under real conditions are quite complex and their characteristics depend on the flow variables required to study. The main difficulty lies in modeling the turbulence, which is characterized by the wide range of temporal and spatial scales, from those generated by tides and bathymetry to those induced by energy recovery devices or the boundary layer at the seabed.

It is common that a complete description of the dynamics of the flow is impractical for engineering problems at high Reynolds numbers in natural bathymetry, so, different degrees of simplification are chosen in the development of numerical models. The detailed study of these flows can be done using Computational Fluid Dynamics (CFD) to plan and supplement experimental research, or for final design of turbines farms under realistic conditions. For this there are different options depending on the complexity, size, and the general objectives of each study.

Statistical models of turbulence based on the Reynolds equations (URANS) can deliver good results for the mean flow at high Reynolds numbers, but are unable to resolve in detail the unsteadyvortices that contains the largest amount of kinetic energy of flow (Paik et al., 2007). On the other hand, spatial filter-based models of the Navier-Stokes equations, called large-eddy simulations (LES), can resolve the dynamics of coherent structures, but computational cost is very high if applied to real cases near the bottom. In these cases it is convenient to implement hybrid models URANS / LES like detached eddy simulations (DES) (Spalart, 2009), which allow to resolve in detail the most important flow scales with moderate computational resources.

The challenges posed by tidal power from the point of view of the turbine design and subsequent implementation are related to the multiple scales of the flow around the devices. Models may incorporate features that go from the detailed design of the blades and the optimal positioning of the turbines within the farm, to changes that may result in the tidal regimes of estuaries, channels and straits.

To develop a proper design for the turbine blade, must be taked in consideration the pressure field and the viscous stress around it. The computational mesh requires a high level of detail to accomplish a proper representation of the blade. Is recommendable the use of modeling techniques that captures the complex dynamics of vortices and coherent structures that develop on the blade. This is subject to the availability of high computational resources or the use of statistical turbulence models that allows a lower resolution of the flow.

Yu, Shen, Zhu, and Du (2010) studied the stall delay phenomenon in the blades of wind turbines. This generates a wrong resolution of the flow with high angles of attack on the blade. Young, ley, and Yeung (2011) coupled the CFD study with a simulation of the transient fluid-structure interaction response, when a turbine is subject to spatially varying inflow. Zanette, Imbault, and Tourabi (2010) studied the mechanical stress sustained by the blade of vertical axis turbines.

The hydrodynamic investigation at medium scale requires models that solve the wake behind the turbine and the possible interactions with the surrounding terrain, like aggradations and scour. They can also manage the interaction with other turbines that form a farm, where many turbines positioned in different ways interact with the local properties of the terrain or some upstream structure that affects the incoming flow in the turbine. This requires computational techniques with less level of detail in the representation of the turbine, but capable of solve the more important coherent structures of the wake.

The chosen techniques for modeling a turbine at this scale are the actuator disk and blade-element momentum (BEM). This techniques have been widely used in wind turbines (Burton et al., 2001). The core of these techniques is to add the effect of the turbine like an actuator disk, applying forces on the flow that represents the devices, but without including the exact geometry of the blade in the computation domain. This technique reduces the computational cost by decreasing the resolution of the mesh in large domains, that include many turbines facing the flow.

One key aspect of the BEM theory is that allows to incorporate elements of turbine design in the actuator disk representation. Some of these elements are the number of blades, the width and pitch angle as a function of the radius. The technique has been used for modeling different situations. Bahaj, Batten, and McCann (2007) and Batten, Bahaj, Molland, and Chaplin (2007), for example, found a good agreement between the theory and experimentation when using a flow with a speeds lower than 2 m/s for different set of configurations.

Myers and Bahaj (2006) found that for some configuration with speeds over 2 m/s the technique underestimates the power output in 140% when is compared with a real scale models. This can be attributed to the stall delay phenomenon. Using a similar model, Antheaume, Maître, and Achard (2008) show a good results when modeling a Darrieus type turbine. This are different from the last ones because it has a vertical axis with respect to the mean flow.

In the line of study of the wake generated by the turbine, the work of Turnock, Phillips, Banks, and Nichollos-Lee (2011), addressed the turbines arrangement within the generation farm. Antheaume, Maître, and Achard (2008) also studied the farm arrangement but for vertical axis turbines. Regarding the modelation of upstream structures, the study of Gaden and Bibeau (2010b) deals with the effect of placing an object upstream of the turbine to improve flow velocity. In a second study (Gaden & Bibeau, 2010a) addressed the effect of diffusers, demonstrating that some structures enhance the power production.

Recent models of wind turbines have used Large Eddy Simulation (LES) to evaluate the effect of the distribution in wind farm and to solve the detail of the coherent structures in the wake. The study performed by Calaf, Meneveau, and Meyers (2010), allows to quantify the vertical transport of momentum and kinetic energy in the atmospheric boundary layer, considering different sub-grid models. A simulation with this level of detail in a complex bathymetry has not been developed for a hydrokinetic turbine in marine current.

A third scale studys the regional effect of the hydrokinetic turbines. The models represent the whole coastal zone where grid size ranges from 50 to 200 meter per square side or even bigger. It consider the effects that a turbine farm has on the whole region, like the change on currents and total volume of fluid carried by the tidal regime. These consequences may have a tremendous impact on the marine species that live in the zone and should be properly quantified for not producing a negative and unexpected impact on the environment.

Some studies use really simplified geometries and hydrodynamics, like the performed by Blanchfield, Garrett, Wild, and Rowe (2008) (Blanchfield, Garrett, Rowe, & Wild, 2008) and Polagye, Malte, Kawase, and Durran (2008) where they studied the energy extraction from a tidal channel linking a bay to the ocean. A extensions of this work also considers far field effects on a network of channels and basins Polagye and Malte (2011).

A parametric representation for the maximum extracted power in a tidal current through a channel was studied by Bryden and Couch (2007) and Garrett and Cummins (2008), the first one focus on the effect of the physical properties of the channel, the second on the partial fences of turbines and the reduction of power due the drag of the devices on the flow. In other study, Vennell (2010) focus on the tuning that the turbine must have in a simplified 1D model, and the number of turbines rows in the farm, showing the increment of drag.

The Regional Models are a methodology for simulate on regional scale, using the geometry, climate conditions and fluid densities (water salinity) of the site. These models use grids with rather large nodes, usually in a 2D simulation or with a few layers on the vertical axis at best case. The node size in a study is around 200 meters or bigger depending on the quality of the site information.

APPENDIX B. CFD 3D MODELING

The purpose of this appendix is to deliver a proper summary of the principal CFD modeling techniques, explaining why different methods are chosen, depending on the complexity of the problem, its size and overall objectives in each study. There are many books that have a deeper look of the topics presented here (Pope, 2000), others with the fundamentals of CFD (Zikanov, 2010), nevertheless the simplicity of this analysis remains.

The turbulence is common phenomenon, usually observed on fluids flows. The everyday examples range from cigarette smoke to planetary scale weather fronts. Nevertheless this flow property is extremely difficult to model and represent, requiring the aid of powerful computer clusters to solve the principal equations that rule the phenomenon. Even today in a so limited form that makes it impracticable in engineering problems, thus requiring different grades of simplification.

The equations mentioned above are the Navier-Stokes equations, with the simplification of incompressible flow, that is appropriate for modeling a flow of water. They are the conservation of mass of flow and the conservation of momentum on each of the three axes. Below are presented, where repeated indices imply sum.

$$\frac{\partial u_i}{\partial x_i} = 0 \tag{B.1}$$

$$\frac{\partial u_i}{\partial t} + u_j \frac{\partial u_i}{\partial x_j} = g_i - \frac{1}{\rho}\frac{\partial p}{\partial x_i} + \frac{\partial}{\partial x_j}\left(\nu \frac{\partial u_i}{\partial x_j}\right) \tag{B.2}$$

Usually the term g_i is added to a the pressure field like a reduced pressure $\bar{p} = \frac{p}{\rho} - g(z_o - z)$ where z_o is a reference for the free surface. So g_i is written implicit in the equations of mass conservation.

Is well known that this set of equations only have explicit solution for a limited number of simplified configurations.The general case do not have a explicit answer. That is the reason why in CFD is so important to use a finite volume or finite differences approach to solve a flow.

This fact opens the question about which is the proper size of the mesh, since it is impossible to capture the movement of an eddy, if this is smaller than the mesh used. Figure B.1 illustrate this in a uniform 2D grid, in blue the eddies that can be represented according to the grid size of the mesh. In red are the eddies with a scale that cant be represented because they are smaller than the size of the grid .

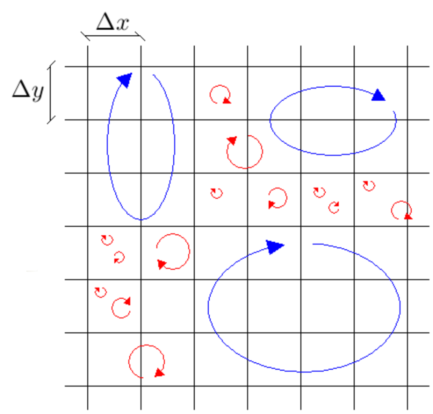

FIGURE B.1. Schematic view of a 2D grid with different sizes eddies.

As with length scale of the grid, the same goes for the time step of the modeling. A motion with a time step smaller than the characteristic time scale of the eddy cannot be represented . This leads to a minimum scale in modeling where the energy of smaller vortex wont be solved in the original set of equations. Here is where the concept of energy cascade introduced by L. F. Richardson in 1922 and later quantified by A. N. Kolgomorov in 1941 takes relevance.

Richardson claimed that ”big whirls have little whirls that feed on their velocity, and little whirls have lesser whirls and so on to viscosity” (Richardson, 1922). The principle says that the energy contained in the larger coherent structures, travels in smaller and smaller eddies, which are generated by the breaking the larger ones, as they are unstable. This process occurs until the energy is transformed into heat by the viscosity, which is able to curb the smaller-scale eddies, whose scale is called Kolgomorov scale (η).

This concept is illustrated on Figure B.2. It has on the horizontal axis the wave number $\kappa(l) = \frac{2\pi}{l}$, which is a measure of the inverse of the characteristic length of the eddies, while the vertical axis demonstrates the energy associated with each wave number. This is an example of a Fourier series analysis of the signal obtained from the measurement of velocity of a point in space.

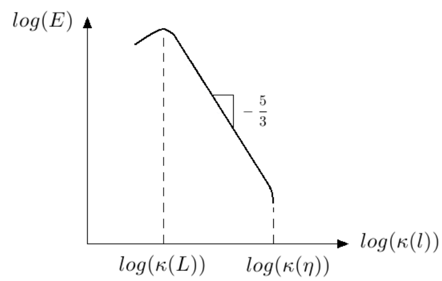

FIGURE B.2. A typical velocity signal that shows the Kolmogorov energy cascade like a Fourier series, where the energy goes from big eddies to the smaller ones.

Thus if the instantaneous velocity is measured in a fixed point in the space, the signal has less turbulent energy, as the size of view window gets closer to the Kolmogorov scale. Also is expected that no turbulent energy would be found on scales smaller that this. Figure B.3 show this.

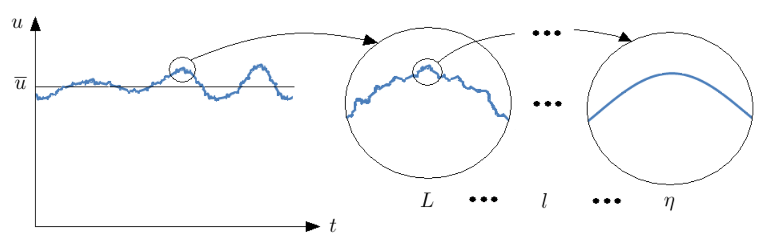

FIGURE B.3. An example of a velocity signal that highlight the energy cascade of Kolmogorov.

Thus the more accurate way of modeling, named Direct Numerical Simulation (DNS), is consequence of trying to reproduce the full motion of the flow, without losing any information due to simplifications. The DNS modeling is achieved with a grid consisting of nodes with length size comparable with η and with a time steps that solves the eddies at this scale.

This kind of modeling gets a accurate description of the flow, for a limited amount of time, solving the Navier-Stokes equation and all the eddies scales that can be present. Is useful for studies of fundamental properties of the turbulance and not aplicable in engeneering problem, as it only solves problems at low Reynolds numbers. Although in the future is expected that the computational resources increases, this wont be enough for a long time to use DNS in practical problems.

Following in level of description, is the Large Eddy Simulation (LES), it only solves the flow that contains the greatest amount of energy, but from some length scale level, the effect is modeled and not solved with the Navier-Stokes equations. Figure B.4 exemplify the modified energy cascade that is obtained with a LES modeling.

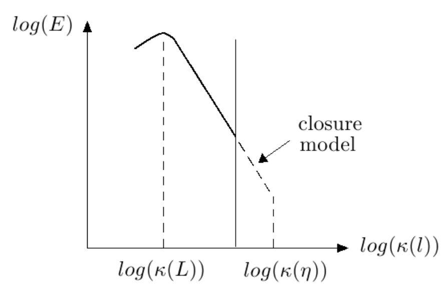

FIGURE B.4. A LES velocity signal like a Fourier series, where the energy goes from the big eddies, to the lenght scale where the energy is not longer solved, and begins to be modeled.

The separation of scales is achived with a mathematical filter on the Navier-Stokes equations. This requires a proper closure for the new terms that arise from the filtering. The objective is that a node that represents a section of fluid in a discrete manner, is able to minimize the error of the discretization from partial derivates and from the filtered small scales.

One way to achieve this is with an explicit LES approach that adds to the governing equations an extra term, which account the filtered smaller scales. A second method is the implicit LES approach, which does not add a new term to the equation, rather it use a numerical method that balance the error from the discretizacin with the error from the missing scales. For a deeper look at the modeling of LES, see the Book of Sagaut (Sagaut, 2006).

LES allows a more suitable configuration of the grids when is compared with DNS. The description is by definition less detailed, but the bigger energetic scales of the turbulence are properly resolved, thus the more important part of the flow is obtained. So LES is suitable for engineering application if computational resources are available.

The next method is the Reynolds average Navier-Stokes (RANS) equations, it achieves a much less detailed description of the flow, because it solve the integrated value in time of the velocity and pressure fields. All the motion of coherent structures is lost in the averaging. The positive part is that allows to solve the bigger engineering problems with moderate computational resources, thats why these methods are available in most modern commercial CFD software.

The first step to achieve this time integration of the Navier-Stoke equations is rewrite the convective term using the conservation of mass equation like $u_j \frac{\partial u_i}{\partial x_j} = \frac{\partial}{\partial x_j}(u_j u_i)$. Next is important to introduce the concept of time average or ensemble average $\overline{a}(t)$, that is the same if the flow conditions are time independent. Considering that the time scale of averaging is much bigger that the time scale present on the flow, then:

$$\overline{a}(t) \quad = \quad \frac{1}{T}\int_{t-\frac{T}{2}}^{t-\frac{T}{2}} a(t')dt' \tag{B.3}$$

(B.4)

The time average has the properties of $\overline{ab} = \overline{a}\overline{b}$ and $\overline{\overline{a}} = \overline{a}$. The time fluctuation of the velocity field u_i' is obtained from time average velocity like $u_i = \overline{u_i} + u_i'$ and is easy to prove with the properties that $\overline{u_i'} = 0$.

The result of applying the time average on the Navier-Stokes equations are:

$$\frac{\partial \overline{u}_i}{\partial x_i} = 0 \tag{B.5}$$

$$\frac{\partial \overline{u}_i}{\partial t} + \frac{\partial}{\partial x_j}(\overline{u_j u_i}) = -\frac{1}{\rho}\frac{\partial \overline{p}}{\partial x_i} + \frac{\partial}{\partial x_j}(\nu \frac{\partial \overline{u}_i}{\partial x_j}) \tag{B.6}$$

The Reynolds stress tensor τ_{ij}, allows a better management of the term $\overline{u_i u_j}$, is defined like:

$$\tau_{ij} = \rho \overline{u'_i u'_j} = \rho \overline{u_i u_j} - \rho \overline{u}_i \overline{u}_j \tag{B.7}$$

From this the RANS conservation of momentum equations are rewritten in their most known form.

$$\frac{\partial \overline{u}_i}{\partial t} + \overline{u_j}\frac{\partial \overline{u_i}}{\partial x_j} = -\frac{1}{\rho}\frac{\partial \overline{p}}{\partial x_i} + \frac{\partial}{\partial x_j}(\nu \frac{\partial \overline{u}_i}{\partial x_j}) - \frac{\partial \tau_{ij}}{\partial x_i} \tag{B.8}$$

The set of equation is not closed because the term $\overline{u'_i u'_j}$ is unknown. An accepted theory for closing it is the Eddy Viscosity Hypothesis, it assume that the turbulent transport depend on a similar way to the mean velocity gradients like the molecular transport depends on the full velocity field (Zikanov, 2010).

The theory is questionable, but the application of this methodology is acceptable for parallel flows. The detail of the multiple closures equations are not shown here. Suffice it to say, that the models most used have one or two equations to estimate the turbulent viscosity ν_τ.

The last ones are the hybrid models, that combine some of the modeling techniques, in this study the technique chosen to solve the flow is the Detached Eddy Simulation (DES), that uses a layer of RANS equations to solve the flow near the wall, and then uses LES on the rest of the domain.

The main advantage of this techniques is that allows a excellent quality of information in the regions of the flow, where the turbines are located and solves a difficulty that LES techniques has on the near wall region. This difficulty is the significant impact that the small scale eddies have a in this region and are filtered with LES. In fact, the closest part of the wall, called viscous sublayer has not turbulent motion. DES is an easy way to solve the near wall flow, mantaining a reasonable demand of computational resources.

APPENDIX C. REPRESENTATION OF THE TURBINES USING ACTUATOR DISKS

For the investigation we use actuator disks to represent the efect of the turbines on the flow. The model is based in theories that uses a series of simplifications for representing the turbines in a parametric way (Burton et al., 2001). Assuming that the disk is located in a perpendicular position to the streamwise direction, can be define V the velocity that the actuator disk faces. This velocity is not equal to the average streamwise velocity, because the disk will slow down the flow in the near upstream section of it, then this velocity is defined as:

$$V = V_\infty(1-a) \tag{C.1}$$

Where V_∞ is the average streamwise velocity upstream of the disk, far from its influence area and a is the axial flow induction factor, that represent the fraction of velocity lost by the current in front of the actuator disk (Burton et al., 2001).

The theory supposed that the turbine is inside a stream-tube as is shown on Figure C.1. Considering the change of momentum experienced by the fluid and some other simplifications (Burton et al., 2001), the theory shows the velocity in the wake will be $V_W = V_\infty(1-2a)$.

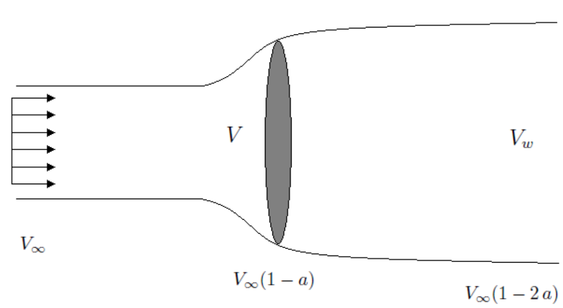

FIGURE C.1. Conceptual model of the flow around the turbine in the actuator disk theory (Burton et al., 2001).

From the conservation of momentum it can be shown that the force applied $\mathcal{F}$ and the power loss $\mathcal{P}$ of the flow by the disk can be written.

$$\mathcal{F} = 2\rho A_d V_\infty^2 a(1-a) \tag{C.2}$$

$$\mathcal{P} = 2\rho A_d V_\infty^3 a(1-a)^2 \tag{C.3}$$

Where ρ is the specific weight of the fluid A_d is the actuator disk area. To characterize $\mathcal{F}$ and $\mathcal{P}$ in dimensionless form, is introduced the thrust coefficient $C_T = \frac{\mathcal{F}}{\frac{1}{2}\rho V_\infty^2 A_d}$ and the power coefficient $C_P = \frac{\mathcal{P}}{\frac{1}{2}\rho V_\infty^3 A_d}$, that are expresen in term of the induction factor:

$$C_T = 4a(1-a) \tag{C.4}$$

$$C_P = 4a(1-a)^2 \tag{C.5}$$

An extention of the model conciders that the fluid gains tangential velocity when it passes through the turbine, because of the spinning of the blades at angular velocity Ω. The fluid acquire a fraction a' of the turbine rotational speed in the center of the disk and two times a' just downstream of the disk (Burton et al., 2001). Taking that in account, the characteristic angular velocity of the wake is defined:

$$\omega = 2\Omega a' \tag{C.6}$$

So the fluid slows down in the axial direction and gains speed in the tangential direction depending on the values of a and a'. Then the rate of change of axial momentum for an annulus of width δr at a distance r of the disk center, corresponds to the force applied on the fluid in the annulus:

$$f_x(r) = 4\pi\rho[V_\infty^2 a(1-a) + (a'\Omega r)^2] r\delta r \tag{C.7}$$

where f_x is the force applied on the annulus in the streamwise direction.

The rate of change in angular momentum in the annulus is equal to the torque applied on the annulus:

$$f_\theta(r) \times r = 4\pi\rho V_\infty(\Omega r)a'(1-a)r^2\delta r \tag{C.8}$$

where f_θ is the force applied on the tangential direction on the annulus.

The forces on the turbine can be represented with equations (C.7) and (C.8), allowing to incorporate the efect of the turbine in the momentum conservation equations. The BEM theory can be used to calculate a and a' from the geometry of the turbine, including the number of blades, its dimensions and the blade pitch (Burton et al., 2001).

The pair of velocities defined in equation (C.1) and (C.6), allows to define the magnitude of the relative velocity on each element of a turbine blade like:

$$V_{rel} \;=\; [V^2 + (\Omega r(1+a'))^2]^{1/2} \tag{C.9}$$

where r is the radial distance from the center of the disk. Figure C.2 shows a perpendicular cut on a radial axis of a blade.

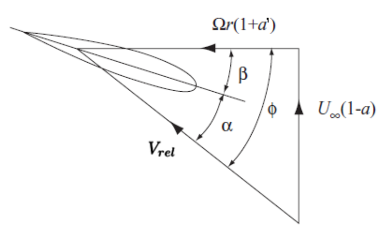

FIGURE C.2. Perpendicular plane to the axis of a turbine blade, with the tangential and streamwise velocity.

If ϕ is the angle between the actuator disk plane and the V_{rel} vector and β the angle between the actuator disk plane and the airfoil zero lift line, then the angle of attack (AoA) α is defined as:

$$\alpha \;=\; \phi - \beta \tag{C.10}$$

$$Tan(\phi) \;=\; \frac{V_\infty(1-a)}{\Omega r(1+a')} \tag{C.11}$$

The drag D and the lift force L that the fluid applies to the blade element, can be calculated like in a 2D aerofoil test. The general formulas for this are:

$$L/u = C_l \frac{1}{2} \rho V_{rel}^2 \, c \tag{C.12}$$

$$D/u = C_d \frac{1}{2} \rho V_{rel}^2 \, c \tag{C.13}$$

where c is the cord length and can change with r, u is the unit lenght perpendicular to the 2D plane, that in this case is δr, C_l and C_d are the airfoil characteristic coefficients.

The force applied on the streamwise direction is calculated $L\ cos\phi + D\ sin\phi$ and in the tangential direction $L\ sin\phi - D\ cos\phi$. Using the 2D airfoil characteristics of blades in combination with the forces on a annulus given by equations (C.7) and (C.8), it can rewrite the two simplified balances of the rate of change in axial momentum and angular momentum like:

$$\frac{V_{rel}^2}{V_\infty^2} N \frac{c}{R} (C_l cos(\phi) + C_d sin(\phi)) = 8\pi[a(1-a) + (a'\lambda\mu)^2]\mu \tag{C.14}$$

$$\frac{V_{rel}^2}{V_\infty^2} N \frac{c}{R} (C_l sin(\phi) - C_d cos(\phi)) = 8\pi\lambda\mu^2 a'(1-a) \tag{C.15}$$

Where N is the number of blades, $\lambda_r = \Omega r/V_\infty$ is called local speed ratio, if $r = R$ the radius of the turbine, then $\lambda_r(R) = \Omega R/V_\infty = \lambda$ is called tip speed radius, c is the chord length and $\mu = r/R$. With a known number of blades N and detailed description of c, C_l, C_d and β as a function of r, equations (C.14) and (C.15) turn in to a closed system for a and a' for a fixed value of λ as a function of r. This allows to add forces of any known turbine geometry like an actuator disk.

The solution given above is no optimal unless the blade geometry is optimized. It can be found a relationship between a and a' just by dividing equations (C.14) and (C.15). Then neglecting the drag and simplifying:

$$a' = \frac{a(1-a)}{\lambda_r^2} \tag{C.16}$$

Maximizing the right side of equation (C.15) using the relationship (C.16) maximizes the torque that each annulus give for a specific λ. The detailed development can be found on (Burton et al., 2001). The optimally designed relationship assumes neglecting the drag, a continuous circulation and requires that there is no radial interaction between annulus, is equal to:

$$a = \frac{1}{3} \tag{C.17}$$

The last results implies that when the optimal conditions are met f_x will be a constant value independent from r by equation (C.7) . Also this particular values for a and a' give a maximum power output known as the best limit, and no turbine in the condition already mentioned can have a better performance. This values allows to calculate the optimal blade geometry by using equation (C.15) , replacing $sen(\phi)$ and neglecting the drag, then simplifying:

$$\frac{Nc}{2\pi R} = \frac{4\lambda\mu^2 a'}{\frac{V_{rel}}{V_\infty} C_l} \tag{C.18}$$

This permits to define the optimal turbine shape, that is Nc/R and ϕ as a function of the radio and λ, although this is not the objective of this work. Assuming that the turbine is optimally designed, equation (C.8) is rewritten, adding the negative drag component that cannot be omitted again, then the torque on the blades elements inside the annulus is:

$$\delta T = 4\pi\rho V_\infty(\Omega r)a'(1-a)r^2\delta r - \frac{1}{2}\rho V_{rel}^2 NcC_d cos(\phi) r\delta r \tag{C.19}$$

$$\delta T = 4\pi\rho V_\infty(\lambda\mu V_\infty)a'(1-a)r^2\delta r - \frac{1}{2}\rho V_{rel}^2 NcC_d \frac{\lambda\mu V_\infty(1+a')}{V_{rel}} r\delta r \tag{C.20}$$

$$\delta T = \frac{1}{2}\rho V_\infty^2 \pi R^3 [8\lambda\mu^3 a'(1-a) - \frac{V_{rel}}{V_\infty}\frac{Nc}{\pi R}\mu^2\lambda C_d(1+a')]\delta\mu \tag{C.21}$$

The above assumes that the turbine adjusts its geometry to λ. This can be true for the pitch angle ϕ but not for the cord length c as a function of the radius. In the case of a fixed design geometry, the next equation would be the same, but with a design fixed value for both a' and λ in the right side of the square brackets and using V_{rel}^2 instead of V_∞^2 (since the designed $\frac{V_{rel}}{V_\infty}$ would be eliminated). Then Replacing (C.18) in (C.21).

$$\delta T = \frac{1}{2}\rho V_\infty^2 \pi R^3 \lambda [8\mu^3 a'(1-a) - 8\lambda\mu^4 a' \frac{C_d}{C_l}(1+a')]\delta\mu \tag{C.22}$$

$$\delta T = \frac{1}{2}\rho V_\infty^2 \pi R^3 \lambda 8[\mu \frac{a(1-a)^2}{\lambda^2} - \frac{\mu^2}{\lambda} a(1-a)\frac{C_d}{C_l} - \frac{a^2(1-a)^2}{\lambda^3}\frac{C_d}{C_l}]\delta\mu \tag{C.23}$$

Integrating across the actuator disk:

$$T = \frac{1}{2}\rho V_\infty^2 \pi R^3 \lambda 8a(1-a)\int_0^1 [\mu \frac{(1-a)}{\lambda^2} - \frac{\mu^2}{\lambda}\frac{C_d}{C_l} - \frac{a(1-a)}{\lambda^3}\frac{C_d}{C_l}]\delta\mu \tag{C.24}$$

$$T = \frac{1}{2}\rho V_\infty^2 \pi R^3 \lambda 8a(1-a)[\frac{1-a}{2\lambda^2} - \frac{C_d}{C_l}(\frac{1}{3\lambda} + \frac{a(1-a)}{\lambda^3})] \tag{C.25}$$

Calculating the power generated by the torque:

$$P = \Omega T = \frac{1}{2}\rho V_\infty^3 \pi R^2 \lambda^2 8a(1-a)[\frac{1-a}{2\lambda^2} - \frac{C_d}{C_l}(\frac{1}{3\lambda} + \frac{a(1-a)}{\lambda^3})] \tag{C.26}$$

From the definition of C_p, where A_d is the area of the actuator disk (πR^2):

$$C_p = 8a(1-a)[\frac{1-a}{2} - \frac{C_d}{C_l}(\frac{\lambda}{3} + \frac{a(1-a)}{\lambda})] \tag{C.27}$$

This is the C_p for an optimally designed turbine that adjust its geometry to any incoming λ. The tip losses were not considerate. Equation (C.8) can be rewritten from the definition of C_p considering the blade characteristics in a easy form to modeling with a computer, like:

$$\delta P = \Omega\delta T = \Omega r \delta f_\theta(r) = C_P \frac{1}{2}\rho V_\infty^3 \delta A_d \tag{C.28}$$

$$\delta f_\theta(r) = C_P \frac{1}{2}\rho \frac{V_\infty^3}{\Omega r}\delta A_d \tag{C.29}$$

A similar development can be done from equation (C.7) to find the value of C_t.

$$\delta F = 4\pi\rho[V_\infty^2 a(1-a) + (a'\Omega r)^2]r\delta r + \frac{1}{2}\rho V_{rel}^2 Nc\, C_d\, sin(\phi)\delta r \tag{C.30}$$

$$\delta F = 4\pi\rho[V_\infty^2 a(1-a) + (a'\Omega r)^2]r\delta r + \frac{1}{2}\rho V_{rel}^2 Nc\, C_d \frac{V_\infty(1-a)}{V_{rel}}\delta r \tag{C.31}$$

$$\delta F = \frac{1}{2}\rho V_\infty^2 \pi R^2[8a(1-a)\mu + 8(a'\lambda\mu)^2\mu + \frac{V_{rel}}{V_\infty}\frac{Nc}{R\pi}C_d(1-a)]\delta\mu \tag{C.32}$$

Making the same assumptions that were made for equation (C.22) and replacing (C.18) in (C.32).

$$\delta F = \frac{1}{2}\rho V_\infty^2 \pi R^2[8a(1-a)\mu + 8(a'\lambda\mu)^2\mu + 8\lambda\mu^2 a'\frac{C_d}{C_l}(1-a)]\delta\mu \tag{C.33}$$

$$\delta F = \frac{1}{2}\rho V_\infty^2 \pi R^2[8a(1-a)\mu + 8(\frac{a(1-a)}{\lambda\mu})^2\mu + 8\frac{C_d}{C_l}\frac{a(1-a)^2}{\lambda}]\delta\mu \tag{C.34}$$

Integrating across the actuator disk:

$$F = \frac{1}{2}\rho V_\infty^2 \pi R^2 8a(1-a)\int_0^1 [\mu + \frac{a(1-a)}{\lambda^2\mu} + \frac{C_d}{C_l}\frac{(1-a)}{\lambda}]\delta\mu \tag{C.35}$$

$$F = \frac{1}{2}\rho V_\infty^2 \pi R^2 8a(1-a)[\frac{1}{2} + b\frac{a(1-a)}{\lambda^2} + \frac{C_d}{C_l}\frac{(1-a)}{\lambda}] \tag{C.36}$$

From the definition of C_t and taking b like the effect of integrating from $\mu = 0.01$. This gives a value for b of 4.6. The induction factor of the first 1 percent of the radius was neglected, assuming that the turbine center adds minimum drag when compared with the whole.

$$C_T \quad = \quad 8a(1-a)[\frac{1}{2} + 4.6\frac{a(1-a)}{\lambda^2} + \frac{C_d}{C_l}\frac{(1-a)}{\lambda}] \tag{C.37}$$

Like in C_p, this C_t is for an optimally designed turbine that adjust its geometry to any incoming λ. The tip losses were not considerate. Equation (C.7) can be rewritten using the definition of C_t considering the blade characteristics. A practical form to modeling with a computer:

$$\delta f_x(r) \quad = \quad C_T\frac{1}{2}\rho V_\infty^2 \delta A_d \tag{C.38}$$

The development of the equations shows different ways of represent the forces based on the quality of the turbine desing information. If the information is minimal, only C_t and C_p are known, then equations (C.38) and (C.29) must be chose. If λ and the 2D shape of the blade is known is better to use (C.37) and (C.27) to calculate Ct and Cp. If the turbine desing is totally characterized, equations (C.14) and (C.15) allows to know a and a' on each annulus, so can add the forces with equation (C.7) and (C.8). This option allows a non-integrated implementation of the equations, more appropiate than the first two cases that result from a averaging.

In this work the forces applied by the actuator disk is represented by f like a force per unit of fluid mass, corresponding at a source/sink of momentum and is expressed as:

$$f = [0,\ f_{x_1},\ f_{x_2},\ f_{x_3}]^T \tag{C.39}$$

The term f_{x_i} is the force per unit of mass in the x_i coordinate. This tems are calculated from the forces applied by the actuator disk. Is important to define the total volume of flow that is affected by this force on each time step. Because the actuator disk represents a porous media, either a porous disk or in the case of a turbine, a time porosity (Nikora, McEwan, et al., 2007), this volume is a fraction of the nodes total volume. Figure C.3 exemplifies the sitiation for a porous media.

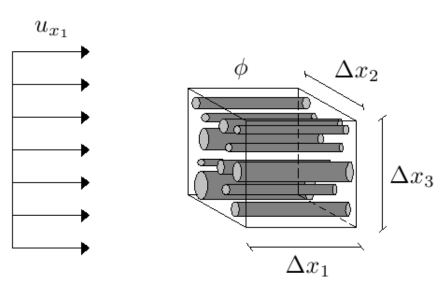

FIGURE C.3. In a node of a porous media the total volume of fluid is reduced to a fraction ϕ.

where u_{x_1} is the velocity perpendicular to the actuator disk, Δx_i are the lengths of the node sides, ϕ is porosity of the media, defined as $\phi = \mathcal{V}_f/\mathcal{V}_0$ where $\mathcal{V}_f$ is the volume occupied by fluid within a region of volume $\mathcal{V}_0$. Then the volume of fluid within a node $\Delta\mathcal{V}ol$ is calculated like:

$$\Delta\mathcal{V}ol = \Delta x_1 \Delta x_2 \Delta x_3 \, \phi \tag{C.40}$$

Using this definition, the force per unit of fluid mass f is calculated from the force applied on the node F_n like:

$$f = \frac{F_n}{\rho \, \Delta\mathcal{V}ol} = \frac{F_n}{\rho \, \Delta x_1 \Delta x_2 \Delta x_3 \, \phi} \tag{C.41}$$

Due equation (C.41), the parameter ϕ has a significant impact on the behavior of the wakes. Is clear that the geometrical properties of the porous medium are averaged within the parameter ϕ, because of that is important to stay open to adjust the parameter to adequately represent the medium, wich can be in this case a porous disc or a turbine.

APPENDIX D. CHANGES IN THE BASE CODE

The original code did not include the option to add the actuator disk forces. This chapter summarizes the changes done on the code that allows to add this forces. This can be useful for anyone wishing to continue this work, use the same code in other application, solve similar problems or better understand how operate this type of software.

The software is based on multiple files.The first file changed was global.f90, this one contains all the global variables. Are add new integer variables: $itur1, itur2, jtur1, jtur2, ktur1$ and $ktur2$. They represent the nodes that surround the center of the turbine, each pair of data can be equal or fix the center of the disk between nodes. Is also add the real tur_{rad} that contains the radius of the actuator disk, and is used to know which nodes are inside the actuator disk zone. The variables has dimension equal to the number of turbines in the simulation $ntur$, that is also added like an integrer on the file.

The last global added is $disk_{dat}$, this variable is not allocated, and would be allocated later. The first two dimensions are the coordinates j and k of the plane in which the disk is set (here the disk is always on a $i = cte$ plane). The last dimension of $disk_{dat}$ is 3, $disk_{dat}(j, k, 1)$, keeps the distance to the center of the disk from the j, k node, if is less than tur_{rad} the rest of the vector will be writen. $disk_{dat}(j, k, 2)$ is called the area factor and keep the dimensionless perpendicular area of the node to the flow, divided by the volume of the node, or one divided by the dimensionless lenght of the node in the flow direcction.

The $disk_{dat}(j, k, 3)$ contains the angle between the line that can be drawn from the center of the disk and goes in the positive Y axis, and, the lines that goes from the center of the turbine toward the center of the node ,only has positive values and uses a counter-clockwise convention.

To the ind3dmg.dat file, was added a set of data in the line 22. The last five lines were lowered one position. The lines added holds the values of $itur1, itur2, jtur1, jtur2, ktur1, ktur2$ and tur_{rad}. If there is more than one turbine, further series are included with more lines.

The file init.f90 was changed to read the new variables in ind3dmg.dat, a read command was added in the read input data section to achive this. Also was added a subroutine $init_{disk}()$, here is where $disk_{dat}$ is calculated from the grid geometry and the new variables of the turbine center position. The calculation requieres the reals $cy, cz, posx, dist, dA, dV$. The first two parameters contain the position of the disk center , in the direction y and z, $posx$ contains the node in the i direction where the disk plane is located.

The file mg driver.f90 was added some global information when the subroutine $solver_{daf}$ is called, in this subroutine everything is solved locally. Each processor has a part of the domain to solve and a local numeration of nodes within it. The information added are ($itur1$ and $itur2$), the global start and end of each processor ($gi_{ia(1)}, gi_{ja(1)}, gi_{ka(1)}, gi_{jb(1)}, gi_{kb(1)}$) and the section of $disk_{dat}$ present in the domain. Then solver daf.f90 is adjusted to receive the incoming data from mg driver.f90. Also the function rhs fd.f90 is called before the call of rhs modale matrices.f90, subroutine that write the left side of the equations.

The only new file added is rhs fd.f90, it travels through all the points (i,j,k) of the local processor and checks if the force should be added, that means if area factor is non equal to zero and if i is equal to the plane of the disk location. Then it adds the dimensionless force applied to the fluid by the turbine, taking in account the distance to the center and the velocity of the incoming fluid. Can also add tangential forces if desired.

The tangential forces are included considering a that the turbines rotate in a clockwise direction, then the forces on the fluid should be added in a clockwise direction. Using the definition of the angle of the position of the node $disk_{dat}(j, k, 3)$, each quadrant would have its own set of equation to add the tangential forces on the x_2 and x_3 directions, Figure D.1 shows this:

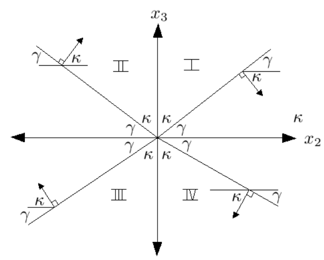

FIGURE D.1. Quadrants that contains the disk have a different equation for the tangential forces based on the angle.

Where γ is the angle from the horizontal axis x_2 to the radius that connect the node to the center of the disk and κ is the angle between the radius and the vertical axis. The equations for the force on each axis for each quadrant, from a tangential force with magnitude F_{tan} are:

$$F_{x_2}^{I} = F_{tan}\, cos(\kappa) \tag{D.1}$$

$$F_{x_3}^{I} = -F_{tan}\, sen(\kappa) \tag{D.2}$$

$$F_{x_2}^{II} = F_{tan}\, cos(\kappa) \tag{D.3}$$

$$F_{x_3}^{II} = F_{tan}\, sen(\kappa) \tag{D.4}$$

$$F_{x_2}^{III} = -F_{tan}\, cos(\kappa) \tag{D.5}$$

$$F_{x_3}^{III} = F_{tan}\, sen(\kappa) \tag{D.6}$$

$$F_{x_2}^{IV} = -F_{tan}\, cos(\kappa) \tag{D.7}$$

$$F_{x_3}^{IV} = -F_{tan}\, sen(\kappa) \tag{D.8}$$

The software can handle nonorthogonal meshes, but to solve the equation must transform the meshes into a orthogonal grid with squares nodes of side 1, this allows a simpler way to solve each equation but must be taken in account for the derivatives. Figure D.2 exemplifies this transformation in a 2D grid.

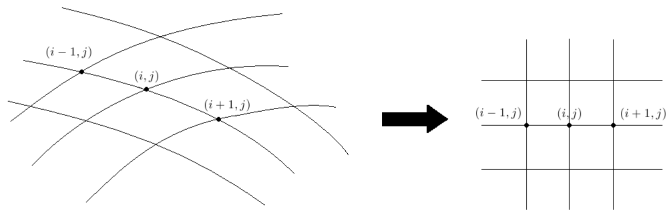

FIGURE D.2. Transformation of a generalized, nonorthogonal curvilinear coordinates to orthogonal square coordinates of side 1 in the 2D case.

In all the last equations the variables are dimensionless with the characteristic lenght $\mathcal{L}$ and flow velocity $\mathcal{U}$. Then the Reynolds number is defined as $Re = \mathcal{U}\mathcal{L}/\nu$ where ν is the cinematic viscocity of the fluid. For clarity a representation of generalized, nonorthogonal curvilinear coordinates are shown on Figure D.3 with the contravarian velocity components.

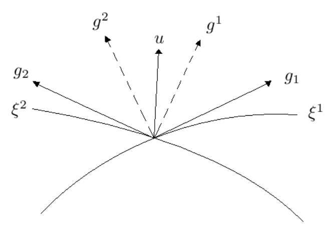

FIGURE D.3. Generalized, nonorthogonal curvilinear coordinates with its corresponding contravariant velocity components.

The resolution of the Navier-Stokes equations is performed writting the right hand side (RHS) similar to equation (17) in (Sotiropoulos & Constantinescu, 1997), plus adjustments considering the non orthogonal curvilinear coordinates. This RHS is defined:

$$RHS \;=\; -(Q^m - Q^n) - \Delta t\, \alpha_m\, R(Q^m) \tag{D.9}$$

where m is the stage of a standard explicit, four-stage, Runge-Kutta procedure, enhanced with implicit residual smoothing (Jameson, , Schmidt, & Turkel, 1981), α_m are the Runge-Kutta coefficients and R is the residual vector which is defined as:

$$R(Q^m) \quad = \quad \left[\frac{\partial}{\partial \xi^j}(F^j - F_V^j)\right]^m \tag{D.10}$$

Thus the turbine force should be inserted inside $R(Q^m)$ to follow the way that the program uses to solve the equations. At the end of solver daf.f90 the subroutine rhs diag solver.F90 multiplies the whole right side by $\Delta t \alpha_m$ and J. So the force is added to $R(Q^m)$ like if it were part of F^j or F_ν^j. For this F_i^j is multiplied by $\xi^j \frac{1}{J}$ in rhs fd.F90, to let the term F_i^j clear when is latter multiplied by $J\frac{\partial}{\partial \xi^j}$. For clarity a summary of the most important subroutines with in solver daf.F90 are shown below.

The solver daf.F90 subroutine is responsible of solve the Navier-Stokes equations. It does it in stages, by calling subroutines that construct the elements of the equation.

Rhs contr j.F90 calculates de contravariant velocity components divided by the Jacobian ($\frac{U^j}{J}$). The pseudo time step is the calculated in rhs daf dtau.F90 this allows to go from $t = t_o$ to $t = t_o + \Delta t$ with a $\Delta \tau$ pseudo time step. The viscous term are calculated on rhs viscous.F90 and rhs diss p.F90 calculate de dissipation on the continuity equation that is the artificial dissipation.

The discretization of the terms Δp Δu is done on rhs flux sans convec.F90 and for the convectives terms is done on rhs convec quick.F90 all this added to $rh(4, i, j, k)$. The no permanent terms of the right hand side ($-(Q^m - Q^n)$) are added on rh unst visc diss.F90 with the others already calculated, this terms are divided by J so they would be in the correct form when multiplied later with the rest of the right hand side.

Here is were the additional turbine forces are added to the right hand side using rhs fd.F90. Then the left side of the equation is calculated in the subroutine rhs modal matrices.F90 and everything is solve on rhs diag solver.F90, thats completes the cycle of the Solver daf.F90 subroutine.

APPENDIX E. VALIDATIONS OF THE MODEL AND DISCUSSION

Two methods were used for the validation of the actuator disk forces. The first one is $in\ situ$ and consists in summing the forces on every node F_n. This forces are defined like:

$$F_n = C_t \frac{1}{2} \rho V_\infty \Delta A \tag{E.1}$$

where ΔA is the area of the plane perpendicular to the flow in the node. If the force is well defined at each node and the size of the disk is properly taken into account, then the sum of all the forces F_n will be equal to the force applied by a disk with geometry given by A_d, a known value of C_t and a state of flux given by V_∞.

The second methodology uses the velocity field obtained from simulations in the virtual channel. Even if the force is revised with the first method, there may have errors in the implementation of the code beacuse the dimensional force should be added in the code as a dimensionless acceleration. The second methodology is the conservation of momentum in the region swept by the turbine that is considered equal to the actuator disk volume and can be expressed by the following equation:

$$\sum F_{ext} = \frac{\partial}{\partial t}\left(\iiint_{\forall} \mathcal{U}\rho \, d\forall\right) + \iint_{S} \mathcal{U}\rho\, \mathcal{U} \cdot \hat{n} \, dS \tag{E.2}$$

where F_{ext} are the volume and surface forces, if the size of the region is well chosen, this value will be nearly identical to the force exerted by the turbine, $\forall$ and S are the volume and surface of the region, $\hat{n}$ is the vector perpendicular to the surface, with a positive value, pointing out of the box and $\mathcal{U} = [u_1, u_2, u_3]^T$ is the velocity field.

The solution is integrated in time, so the first term on the right side is equal to zero. The viscous stresses are considered on this analysis but a large portion of the area in the region is perpendicular to the flow, so the viscous stresses on that area do not affect the conservation of momentum in the direction of the force used to calculate C_t. The loss of momentum due the turbulence is neglected because the region considered has a small total volume due its small width. So the equation used is:

$$\mathcal{F} + \mathcal{P} \;=\; \iint\limits_{S} \mathcal{U}\rho\,\mathcal{U} \cdot \hat{n} dS \tag{E.3}$$

where $\mathcal{F}$ is the force applied by the actuator disk and $\mathcal{P}$ is the total force generated by the pressure in the zone. The velocity used has to take in account the porous media in the disk zone. So if the average velocity in a node of area ΔA is U_x, in this analysis the area will be $\Delta A\ \phi$ and the velocity U_x/ϕ due to mass conservation, where ϕ is the porosity.

Three values of C_t recorded in laboratory experiments (Myers & Bahaj, 2010) were choosen to perform the validation. The C_t values are 0.61, 0.86 and 0.94. Later simulations were performed and the comparison between the theoretical values of C_t and the results of calculating $C_t\ insitu$ and the $C_t\ field$ are shown in table E.1.

C_t	$C_t\ insitu$	$C_t box$
0.61	0.609	0.667
0.86	0.858	1.143
0.94	0.938	0.961

TABLE E.1. Theoretical values of C_t and the results of calculating $C_t\ insitu$ and the $C_t\ field$ from the simulations.

The result shown good agreement between C_t and $C_t\ insitu$ with a maximum error of 0.216% in the case of $C_t = 0.86$. This shows that the actuator disk geometry, the mesh and the upstream flow conditions are duly taken in account for the calculation. Indeed the $C_t\ insitu$ value includes the geometry of the nodes within the actuator disk and the upstream conditions of the flow due to the equation (E.1). This minimun error can be explained beacuse a rectangulare grid is used to represent a disk and also due minimal differences between the simulated and measured velocity profile upstream the disk.

The agreement between C_t and $C_t\ field$ is lower than with $C_t\ insitu$, with a maximum error of 24.6% in the case of $C_t = 0.86$. The error implies that for $C_t = 0.86$ the averaged flow field behaves as if the force applied was of a magnitud 24.6% larger than it should. The second largest is for $C_t = 0.61$ with an error of 8.6%. The causes for this increases in the forces is an improper calibration of the porosity parameter ϕ, that overstate the effect of the force when is transformed in to an aceleration per unit of mass, see equation (C.41). The calibration for the case $C_t = 0.94$ is near the optimun, with a small error of 2.19%. The transformation performed to include the force in the equations like a dimensionless acceleration is properly done by the code, but it is always important to adjust the parameter ϕ.

The features that is wanted to recreate with the simulations are the shapes of the wakes. They are described by the length of the wake and amount of momentum that the flow recovers, as it moves away from the turbine. To compare this, the flows are averaged in time and then a velocity deficits parameter is calculated. The velocity deficits is defined as:

$$\mathcal{U}_{def} = 1 - \frac{\mathcal{U}_1}{\mathcal{U}_0} \tag{E.4}$$

where $\mathcal{U}_0$ is the velocity if the turbine is not affecting the flow and $\mathcal{U}_1$ is the velocity when the turbine is included in the fluid (Myers & Bahaj, 2010).

Figure E.1 shows the velocity deficits for the three cases studied by Myers and Bahaj (2010) and the results of the CFD model. Because the solutions are time integrated, the coherent structures are not clearly visible. The porosity was used to calibrate the simulations with the measured wakes, to obtain the most similar shapes. The values of ϕ are equal to 0.13, 0.30 and 0.3655 for C_t values of 0.61, 0.86 and 0.94 respectively.

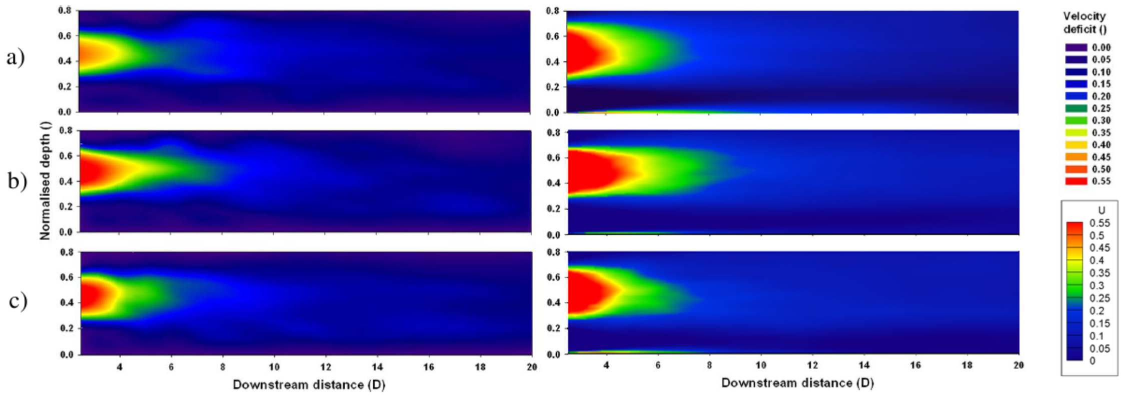

FIGURE E.1. Comparison of the velocity deficit in center plane of the wake between measurements (Myers and Bahaj, 2010) and the results from the simulation with C_t values of a) 0.61, b) 0.86 and c) 0.94.

The results are fairly good, showing similarity for the three values of C_T despite the fact that the differances in the C_t box parameter and the difficulty of adjust the color band of the results of the simulations, with the one used for the measurements (Myers & Bahaj, 2010). The wakes in b) are slightly larger than for the other C_t values, for both the measurements and the simulations. The cases a) and c) have a similar lenght and width of the wake, for both the measurements and the simulations. A plot of the centerline velocity deficit is presented on Figure E.2 for the three values of C_T considered.

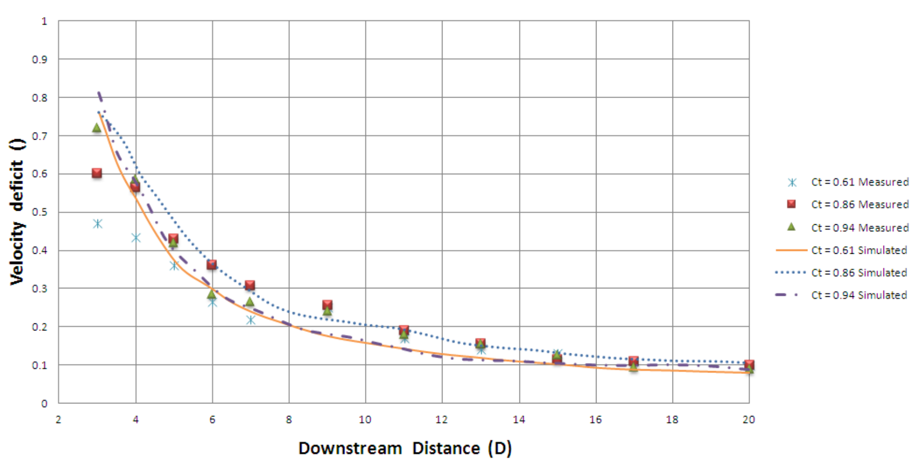

FIGURE E.2. Plots of the centerline velocity deficit from the model with the values of the measurements (Myers and Bahaj, 2010) with C_t values of 0.61, 0.86, 0.94.

Similar to (Myers & Bahaj, 2010) the results show a convergence of the plots, that occours when the distance is larger than 10 and 15 diameters downstream (D) in the case of the measurements and simulation respectively, because the shape of the far wake region is dominated by the ambient turbulence.

The simulation for the case $C_t = 0.94$ describes the first 7D properly, with a good desription of the near wake zone, that is between 0 to 5D, then it has an error of order 5% until 15D where it regain a more suitably description. For $C_t = 0.86$ is the opposit, the description is proper from 6D onwards, while the near wake zone has important differances. In the case $C_t = 0.61$, the description is improper for 3D, for 4D the error is of order 6% and onwards the description is adequate. The error in the representation of the near wake zones is aceptable, beacuse a porous disk cannot generate the same coherent structures than a turbine.

The instability on Figure E.2, can be explained beacuse of the time integration interval of the simulations, which corresponds to a minimum of 2000 time steps, ie 20 dimensionless seconds. This amount may be too small, so it generates the instability.

This results for the time-average fields means an advance in the simulation of hydrokinetic turbines with actuator disks using LES, because the authors have not found other studies that achieve this goal even with a lower degree of accuracy.

Figure E.3 shows a comparison for the velocity deficits between the measurements at the left side and the simulations in the right side, using the same disk centered at a height of a) 0.75, b) 0.66 and c) 0.33 (Myers & Bahaj, 2010). This values are normalised with the height. The C_t value used is 0.86 and the ϕ value is 0.3.

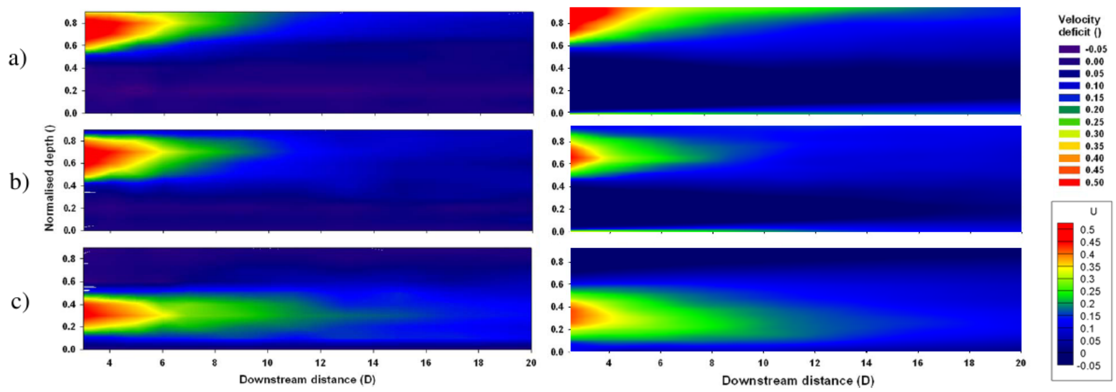

FIGURE E.3. Velocity deficit in center plane of the wake for the measurements (Myers and Bahaj, 2010) and the results from the simulations with the center of the porous disk and a actuator disk located at a height of a) 0.75, b) 0.66 and c) 0.33.

The simulation c) with the disk at lower height shows a wake that regains its velocity slower than the case b) located at 0.66, which is consistent with the measurements. The plots b) and c) are consistent for the total lenght of the wake, but shows a shorter red zone for the simulations in the near wake region, while in the measurements the red zone is much longer. The difference can be explain by the uncertainty of not knowing the value taken by the parameter C_t in these measurements, the challenge to simulate the near wake region plus the difficulty to set the colors at the same scale used by the Myers and Bahaj (2010). The simulation at a) shows a greater wake in the upper part. This can be generated by the lower transport and mixing, than this zone has when is compared with the measurement. The model cannot change the free surface as it happens in reality. This limitation can explain the lower transport and mixing on the upper part that generates an deformation of the wake. These results shows the capacity of the model to simulate the extraction of energy at different hights at the water column. The site selection of the turbines farm must consider the increase of the wakes at low height, that increases the farm size and reduces its power output.

The interactions between two or more turbines are critical in farm arrangement. An optimal distance leads to an increment of the velocity passing trough the turbines, while an inadequate setting can enhance the wakes lenght. A previous study found that the velocity between turbines can increases 10% at the second row of the farm (Myers & Bahaj, 2012). This implies an increment of 30% in power, due to the cubic relationship between velocity and power. Simulations with two turbines are compared with porous disks measurements (Myers & Bahaj, 2012) in Figure E.4.

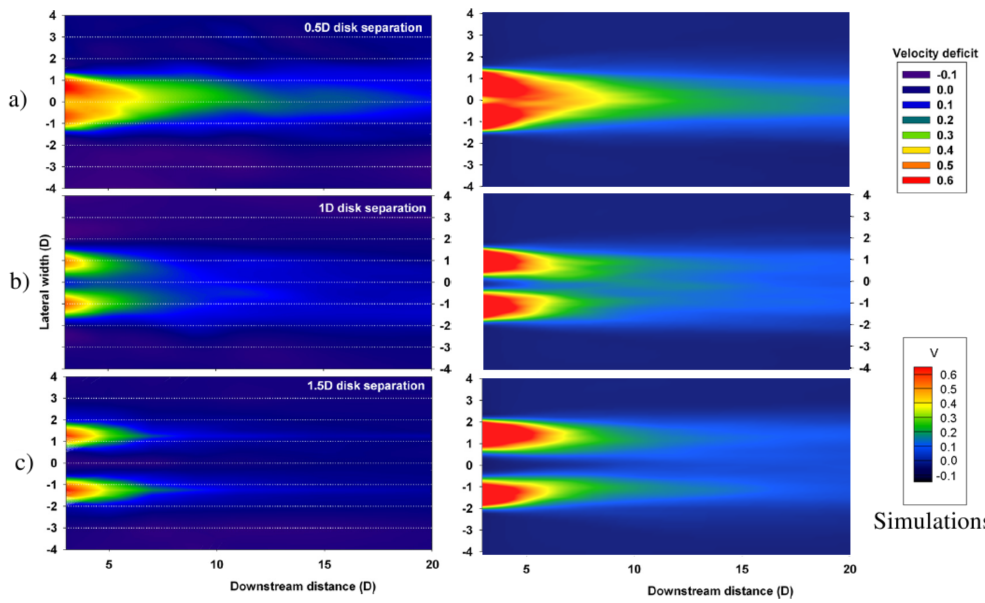

FIGURE E.4. Comparison of the velocity deficit in a plan view of the center plane of the wakes generated by two turbines, between the measurements (Myers and Bahaj, 2012) and the results of the simulations with a separation of a) 0.5D, b) 1.0D and c) 1.5D between porous and actuator disks.

The result show a roughly similar behavior despite that the measurement were recorded using a disk with C_t equal to 0.91 and unknown porosity, while the simulations are performed using a C_t value of 0.94 and ϕ equal 0.3655. This values were choosen from the already calculated and validated, because they are the closer to the new case. This may produce differances in the shape of the wakes.

In the case a) with a disk separation of 0.5D, the wakes merge in a larger one, in the simulation and the measurement. The shape of the combinated wakes is rougly similar, but longer in the simulation.The Case b) with a separation of 1.0D, shows how the wakes partially merge, without an important flow between the turbines. As in a) the wakes in the simulation are longer. Case c) with a separation of 1.5D, leaves enough room between the turbines so the flow goes through them and accelerates, allowing the wakes to follow independently. The velocity between them increases 7% in the measurements and 6.7% in the modeling at 3D downstream from the turbines when is compared with the free flow condition. This capacity to properly reproduce the interactions of two or more turbines is a key element to model farm arrangments. In the three cases the simulations has longer wakes, this is explained by the differances in C_t mentioned in the study of a single turbine located at different heights.

The previos analisys is performed with the mean flow statistics, hidding the rich dynamic behavior of the flow, compound by coherent structures motion. Compare the turbulence statistics of the flow allows a deeper look at the behaviour of the wakes and swirls.

A Reynolds stress analisys allows to compare the importance of the transport of momentum from a fast moving zone, to region with lowered velocity, that in this case is the wake. Figure E.5 show the resolved Reynolds stress for a centerplane in simulation of a turbine with it center located at 0.33 dimensionless height.

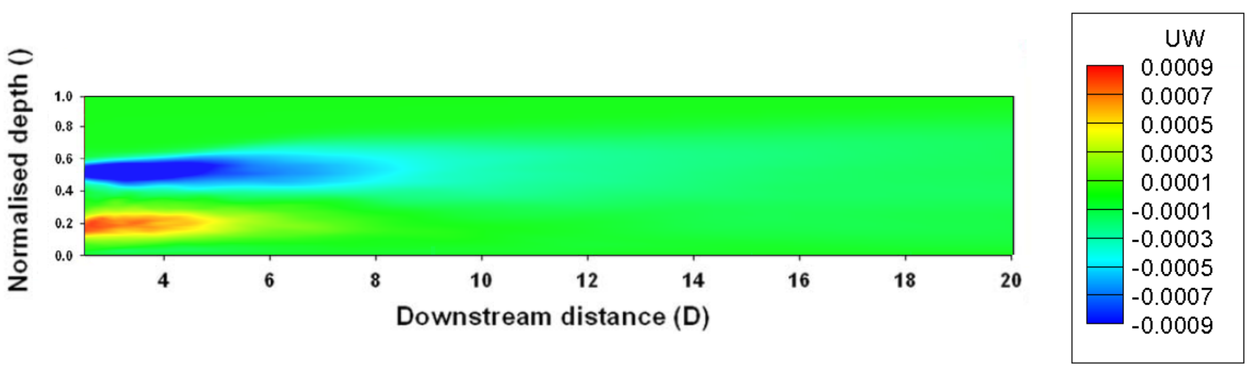

FIGURE E.5. Centerplane of the solved Reynolds stress (m^2s^{-2}) of a simulation with the center of the actuator disk located at 0.33 dimensionless height, $C_t = 0.94$ and $\phi = 0.3655$.

The simulation reproduces the lack of vertical symmetry of Reynolds stress shown in the measurements (Myers & Bahaj, 2010). The model is able to simulate wakes that are not axisymmetric. Also the simulation agrees with the measurement in the gradually dissipation of the shear stress, having a non symmetrical value even at a distance of 9D (Myers & Bahaj, 2010). Regarding the size of the Reynolds stress, there are differances between the simulation and the measurements. For the peak value measured in 3D, the simulation shows a value 4 times greater. At 20D from the turbines, the values are homogeneous like in the simulations, but with twice as large. This disagreement can be caused because the Reynolds stresses are from the solved part of the simulation. This means that none of the sub-grid motions that are solved by the turbulance model, are taken in account, due that the turbulance model cannot provide that information.

A similar analysis is performed for the turbulent kinetic energy per unit of fluid mass (TKE) solved in the simulation. Similar to Reynolds stress , this parameter not take into account the contributions of the turbulance model, that solves the sub-grid scale eddies. The TKE is measurement of the intensity of the turbulance. The definition of TKE is:

$$TKE = \frac{1}{2}\left(\overline{u_i' u_i'}\right) \tag{E.5}$$

where $\overline{\bullet}$ is the time average operator, u_i' are the components of varition of the velocity given a by Reynolds decompotitions. Figure E.6 shows a centerplane of the solved dimensionless TKE of the flow through and actuator disk with the same configuration used in Figure E.5.

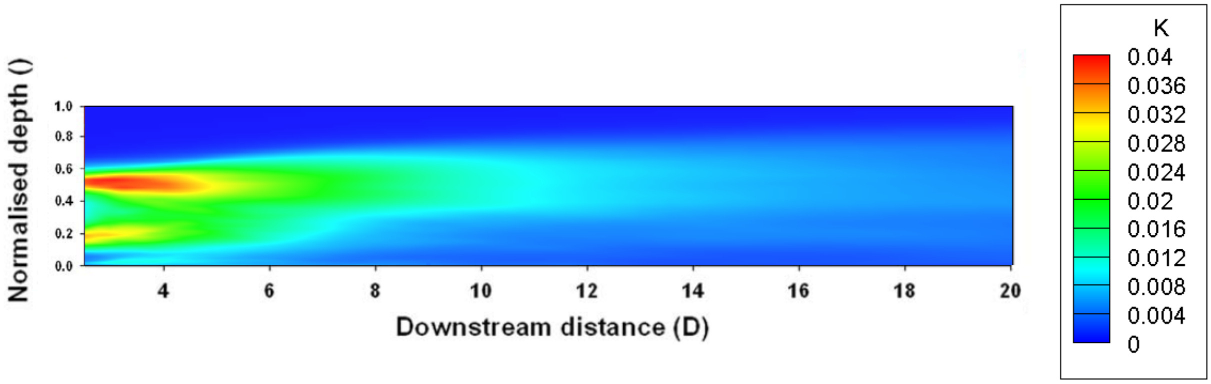

FIGURE E.6. Centerplane of solved dimensionless TKE of an actuator disk centered at 0.33 dimensionless height, $C_t = 0.94$ and $\phi = 0.3655$.

The vertical assymetry of the flow turbulance is confirmed with the result of the TKE. In the measurements (Myers & Bahaj, 2010), the results shown a symmetric vertical distribution of the TKE. This discrepancy in the shape of the distribution can be generated by the low resolution of the data measure in the vertical axis, that is at every 10% dimensionless height. Figure E.7 shows that the actuator disk set on a higher position, 0.5 dimensionless height, develops a symetric vertical distribution, like the ones described on the measurements (Myers & Bahaj, 2010). The red zone of high TKE develops in evenly above and below the actuator disk, in contrast the actuator disk located at lower portion of the flow, develops a stronger red zone in the upper part.

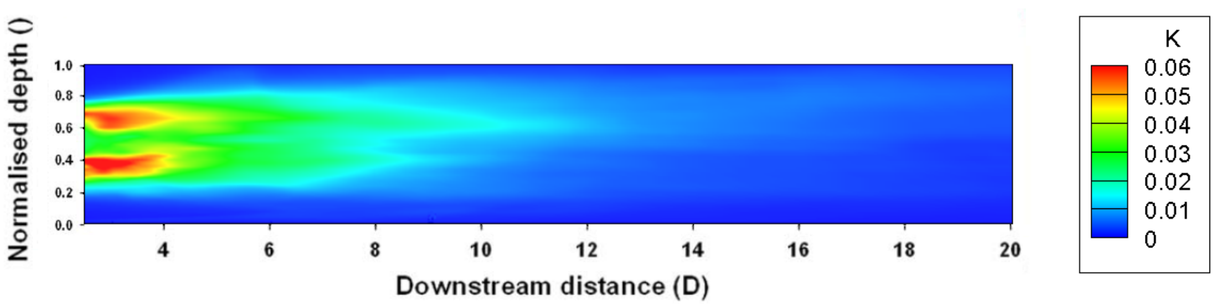

FIGURE E.7. Centerplane of solved dimensionless TKE of an actuator disk centered at 0.5 dimensionless height, $C_t = 0.94$ and $\phi = 0.3655$.

Regarding to the value of the TKE, a previous study (Paik et al., 2007) using the same model and R_e in the order of magnitud, found similar values of the resolved TKE. There are multiple challenges to compare this values of TKE. The first one is that the TKE simulated by the turbulance model is lost, also that actuator disk shape, as is the distribution of holes, can has a significant impact in the flow movement in the near wake region (distances $< 5D$), aditionally the presence of the instrumental error in the record of the measurements. An in-depth comparison of the TKE generated by different actuator disks is beyond the scope of this paper and will be left as a subject for future work.

APPENDIX F. POWER SPECTRAL DENSITIES

For the signal analysis the series is split in 12 parts, then a Fast Fourier tranformate (FFT) is applied on each part of the signal and the 12 results are averaged. This removes the noice on the signal. Figure F.1 shows the FFT for the three componenets of cartesian velocity in the five points with a data.

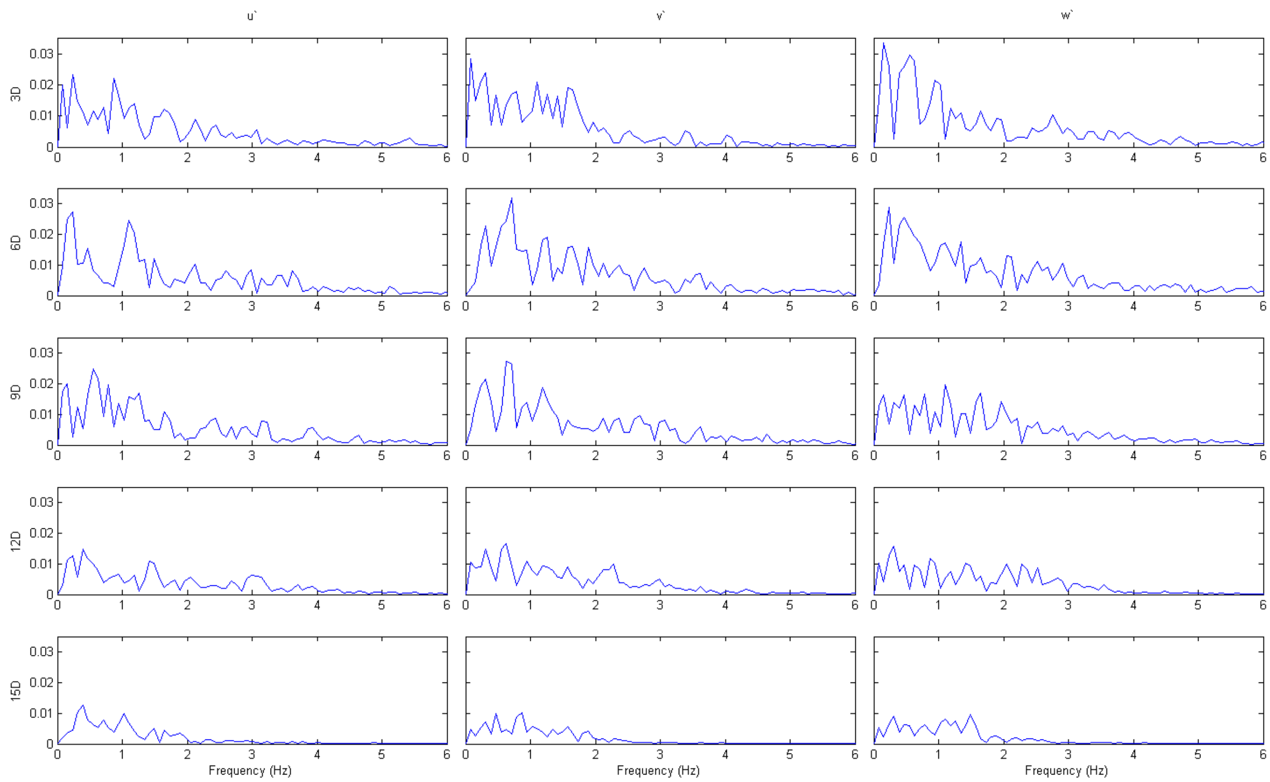

FIGURE F.1. FFT of the components of cartesian velocity from series recorded at 3D, 6D, 9D, 12D and 15D.

APPENDIX G. FROM MEDIUM SCALE TO REGIONAL MODELING

Regional models have large grids and turbines are contained entirely within the elements of the discretization. The wakes in these cases are represented by a small number of nodes. Here the effect of the turbine implies a sub grid effect, beacuse the distribution of velocities inside the nodes is very complex, while in finite elements it is assumed that the velocity is represented by a central value of the nodes and a interpolated value for the edges of them.

Figure G.1 exemplifies this modeling situation, where a few nodes represent a flow going trough a turbine, here the central averaged value is not enough information to represent the flow, due the shape of the wake. A proper way to aggregate the information from a detailed 3D medium scale model is like a sub grid effect, using the $Doble\ Average\ Navier\ Stokes$ (DANS) equations (Nikora, McEwan, et al., 2007; Nikora, McLean, et al., 2007).

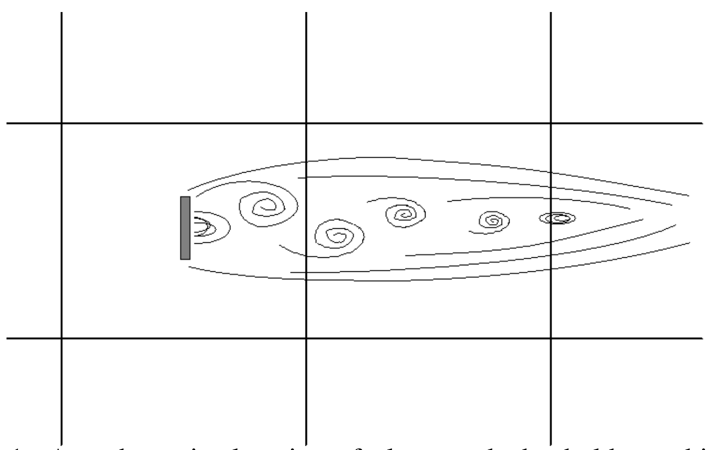

FIGURE G.1. A a schematic plan view of a large node that holds a turbine and part of the wake inside of it.

The DANS equations are a extension of the RANS equations. Are obtained by averaging the $Navier\ Stokes$ equations in the volume, thus the averaged volume goes from a detailed description of the velocity field, to a single averaged velocity value on each direction. If the node holds elements different from the fluid, the geometric properties of this elements are lost in the averaging, beacuse the velocity description cannot be smaller than the node size, then the flow around this elemenets cannot be representated.

After applying the DANS equations, all the sub grid structures also disappears from the mesh, as they cannot be geometrically represented. The meshes become simpler due the second averaging of the DANS equations. All this simplifications has to take in account the effect of the elements on flow, allowing to represent the flow correctly despite the nodes size. This requires additional terms in the equations to represent the effect of the averaged elements.

The uses of this technique range from a representation of sediments in the flow, bed roughness, vegetation, and if the scale is big enough, turbines in a channel. By using RANS equations the meshes do not need to adjust to bedformes, leaves of plants, algaes, rocks or turbine blades, allowing to consider this elements, but at a low computational cost due the use of less nodes into the mesh.

Two spatial averages (Nikora, McEwan, et al., 2007) are introduces, the intrinsic spatial average $\langle\theta\rangle$ and superficial spatial average $\langle\theta\rangle_S$:

$$\langle\theta(x, y, z, t)\rangle = \frac{1}{\mathcal{V}_f}\int_{\mathcal{V}_f}\theta d\mathcal{V} \tag{G.1}$$

$$\langle\theta(x, y, z, t)\rangle_s = \frac{1}{\mathcal{V}_o}\int_{\mathcal{V}_f}\theta d\mathcal{V} \tag{G.2}$$

where θ is a flow variable, $\mathcal{V}_f$ is the volume occupied by fluid in the averaging zone with total volume equal to $\mathcal{V}_o$. The DANS equations are obtained of applying these averages to the RANS equations (Nikora, McEwan, et al., 2007). So the DANS equations are averaged in time $\overline{\bullet}$, then in space $\langle\bullet\rangle$ and are equal to:

$$
\begin{aligned}
\frac{\partial\langle\overline{u}_i\rangle}{\partial t}+\partial\langle\overline{u}_i\rangle\frac{\partial\langle\overline{u}_i\rangle}{\partial x_j} &= g_i-\frac{1}{\rho\phi}\frac{\partial\phi\langle\overline{p}\rangle}{\partial x_i}-\frac{1}{\phi}\frac{\partial\phi\langle\widetilde{u}_i\widetilde{u}_j\rangle}{\partial x_j}-\frac{1}{\phi}\frac{\partial\phi\langle\overline{u_i'u_j'}\rangle}{\partial x_j}\\
&+ \frac{1}{\phi}\frac{\partial}{\partial x_j}\phi\left\langle\overline{\nu\frac{\partial u_i}{\partial x_j}}\right\rangle+f_{p_i}+f_{\nu_i} \qquad \text{(G.3)}\\
\rho\frac{\partial\phi}{\partial t}+\rho\frac{\partial\phi\langle\overline{u}_i\rangle}{\partial x_i} &= 0 \qquad \text{(G.4)}
\end{aligned}
$$

where $\phi=\phi_s\langle\phi_t\rangle$ combines the effect of the spatial porosity $\phi_s=\mathcal{V}_f/\mathcal{V}_o$ and the time porosity $\phi_t=T_f/T_o$, accounting the relationship between the total time in the averaging interval T_o, and the total time that the averaged node is only with fluid T_f. This time porosity allows to represent moving elements, like plants waving in a stream or turbine blades rotating.

The form drag per unit fluid volume f_{pi} and the viscous drag per unit of fluid volume $f_{\nu i}$ holds the effects of the forces due pressure and the viscous stresses respectively, applied by the subgrid elements. Usually they are calculated from a drag force $C_T\frac{1}{2}\rho V_\infty^2 A_d$, with known value of C_t for spheres, cylinders and the actuator disks.

When the turbine is contained completely within an element of the discretization, the term ϕ_s can be reasonably approximated to 1, because the volume of the turbine blades and center are a small fraction of the node total volume. The term ϕ_t cannot be approximated to 1 in an intermediate node swept by the blades. In a regional model, this contribution disappears due the larger volume surrounding the turbine, containing only fluid at all times. This allows to consider $\phi_t=1$ for these element of the discretization. This simplifies the value of ϕ to 1 on the DANS equation for the regional model.

The term of temporal fluctuations appears when the time integration is performed to calculate the RANS equations, by using the Reynolds decomposition $u_i=\overline{u_i}+u_i'$. In a similar form a spatial fluctuation appears, due the Grays decomposition $\overline{u_i}=\langle\overline{u_i}\rangle+\widetilde{u}_i$ (Gray, 1975). The form-induced stress $\langle\widetilde{u}_i\widetilde{u}_j\rangle$ appears when the RANS equations is spatially integrated and is an unknown that needs a closure.

In the case of $\overline{u_i'u_j'}$, the mayority of CFD software including ROMS, solve it with the $k-\varepsilon$ set of two equations (Wilcox, 1994). They are a closure model for the turbulance, that allows to represent the transport of kinetic energy k from the flow and also the transport of the dissipation of energy ε. These equations require a definition for a series of parameters, that are obtained empirically.

The basic hypothesis for $k-\varepsilon$ is that the Reynolds stress tensor can be calculated using a Turbulent viscosity model (Pope, 2000), the model states that:

$$\overline{u_i'u_j'} = -\nu_T \frac{\partial \overline{u_i}}{x_j} \tag{G.5}$$

where ν_T is the turbulent viscosity thats relates to k and ε using the equation:

$$\nu_T = C_\mu \frac{k^2}{\varepsilon} \tag{G.6}$$

where C_μ is one of the five parameters determinated empirically, with a value of 0.09. The transport equations for k and ε are:

$$\frac{\partial k}{\partial t} + \overline{u}_i \frac{\partial k}{\partial x_j} = -\overline{u_i'u_j'} \frac{\partial \overline{u}_i}{\partial x_j} - \varepsilon + \frac{\partial}{\partial x_j}\left[(\nu + \nu_T/\sigma_k)\frac{\partial k}{\partial x_j}\right] \tag{G.7}$$

$$\frac{\partial \varepsilon}{\partial t} + \overline{u}_i \frac{\partial \varepsilon}{\partial x_j} = C_{\varepsilon 1}\frac{\varepsilon}{k}(-\overline{u_i'u_j'})\frac{\partial \overline{u}_i}{\partial x_j} - C_{\varepsilon 2}\frac{\varepsilon^2}{k} + \frac{\partial}{\partial x_j}\left[(\nu + \nu_T/\sigma_\varepsilon)\frac{\partial \varepsilon}{\partial x_j}\right] \tag{G.8}$$

where $C_{\varepsilon 1} = 1.44$, $C_{\varepsilon 2} = 1.92$, $\sigma_k = 1.0$ and $\sigma_\varepsilon = 1.3$. This is an closure model for the turbulent transport equations, that does not include sub-grid effects. In that case $\langle\rangle$ is surplus.

The proposed methodology to deal with the tensor $\langle \widetilde{u}_i \widetilde{u}_j \rangle$ is to calculate the value directly from the 3D simulation, integrating in time all the turbulent motion given by the

DES simulation, then calculating the values of the spatial variation of the velocity $\widetilde{u}_i$, on every node that is inside the regional model node (rmn). The equation used is:

$$\langle \widetilde{u}_i \widetilde{u}_j \rangle_{rmn} = \sum_{i,j,k} \langle \widetilde{u}_i \widetilde{u}_j \rangle_n \mathcal{V}_n(i,j,k) / \mathcal{V}_{rmn} \tag{G.9}$$

where i,j,k denote a field of elements of discretization, which are within a regional model node, $\langle\rangle_n$ and $\mathcal{V}_n(i,j,k)$ are the spatial averaging and volume of the field of elements of discretization, $\mathcal{V}_{rmn}(i,j,k)$ and $\mathcal{V}_{rmn}$ are the spatial averaging and volume of the regional model node.

This methodology allows to consider the turbine geometry, configuration and the sub grid topography in the regional model. As a example the tensor $\langle \widetilde{u}_i \widetilde{u}_j \rangle_{rmn}$ is calculated for an rectangular channel used in the validation, the units are $(m^2 s^{-2})$, the C_t parameter is equal to 0.86, the actuator disk center is located on the center of the node, that is square-shaped with side of 3D:

$$\langle \widetilde{u}_i \widetilde{u}_j \rangle_{rmn} = \begin{bmatrix} 1.42 * 10^{-4} & -2.00 * 10^{-7} & 5.28 * 10^{-6} \\ -2.00 * 10^{-7} & 4.28 * 10^{-5} & 3.15 * 10^{-7} \\ 5.28 * 10^{-6} & 3.15 * 10^{-7} & 4.37 * 10^{-5} \end{bmatrix} \tag{G.10}$$

A $\langle \widetilde{u}_i \widetilde{u}_j \rangle_{rmn}$ for a free stream flow upstream of the actuator disk is shown in equation (G.11), allowing to appreciate the differances when is compared with the regional node that holds the actuator disk on its center.

$$\langle \widetilde{u}_i \widetilde{u}_j \rangle_{rmn} = \begin{bmatrix} 4.28 * 10^{-9} & 7.96 * 10^{-11} & -5.28 * 10^{-10} \\ 7.96 * 10^{-11} & 1.21 * 10^{-9} & 5.45 * 10^{-11} \\ -5.28 * 10^{-10} & 5.45 * 10^{-11} & 2.78 * 10^{-10} \end{bmatrix} \tag{G.11}$$

Rewriting the equations (G.3) and (G.4) with consideration of ϕ equal to one, the simplification of using the drag force and the Turbulent viscosity model, plus a known value of $\langle \widetilde{u}_i \widetilde{u}_j \rangle_{rmn}$, and $k - \varepsilon$ model of CFD sofware, turns in to a closed DANS model:

$$\begin{aligned}
\frac{\partial \langle \overline{u}_i \rangle}{\partial t} + \partial \langle \overline{u}_i \rangle \frac{\partial \langle \overline{u}_i \rangle}{\partial x_j} &= g_i - \frac{1}{\rho} \frac{\partial \langle \overline{p} \rangle}{\partial x_i} - \frac{\partial \langle \overline{u_i' u_j'} \rangle}{\partial x_j} + \frac{\partial}{\partial x_j} \left\langle \overline{\nu \frac{\partial u_i}{\partial x_j}} \right\rangle \\
&- \frac{\partial \langle \widetilde{u}_i \widetilde{u}_j \rangle_{rmn}}{\partial x_j} - C_{Ti} \, \frac{1}{2} \langle \overline{u}_i \rangle^2 A_d \qquad \text{(G.12)} \\
\rho \frac{\partial \langle \overline{u}_i \rangle}{\partial x_i} &= 0 \qquad \text{(G.13)}
\end{aligned}$$

If the site topography is known and the farm characteristics defined, is possible to calculate tensors $\langle \widetilde{u}_i \widetilde{u}_j \rangle$ as function of the flow velocity. Change the equations on CFD softwares like ROMS, to (G.12) and (G.13) requires adding of the last two terms of the right side of (G.12). This would allows a better representation of the hydrodynamic processes that occur on the site, incorporating the sub-grid effects starting from a detailed model.